

NUREG/CR-3662
SAND81-0413
R7
Printed October 1983

Fuel-Disruption Experiments Under High-Ramp-Rate Heating Conditions

S. A. Wright, D. H. Worledge, G. L. Cano,
P. K. Mast, F. Briscoe

Prepared by
Sandia National Laboratories
Albuquerque, New Mexico 87185 and Livermore, California 94550
for the United States Department of Energy
under Contract DE-AC04-76DP00789

BEST AVAILABLE COPY

Prepared for
U. S. NUCLEAR REGULATORY COMMISSION

* TOTAL PAGES: 88
* Includes all paginated
+ non-paginated pages in
various pagings.

NOTICE

This report was prepared as an account of work sponsored by an agency of the United States Government. Neither the United States Government nor any agency thereof, or any of their employees, makes any warranty, expressed or implied, or assumes any legal liability or responsibility for any third party's use, or the results of such use, of any information, apparatus, product, or process disclosed in this report, or represents that its use by such third party would not infringe privately owned rights.

Available from
GPO Sales Program
Division of Technical Information and Document Control
U.S. Nuclear Regulatory Commission
Washington, D.C. 20555
and
National Technical Information Service
Springfield, Virginia 22161

NUREG/CR-3662
SAND81-0413
R7

FUEL-DISRUPTION EXPERIMENTS UNDER
HIGH-RAMP-RATE HEATING CONDITIONS*

S. A. Wright
D. H. Worledge**
G. L. Cano

Sandia National Laboratories
Albuquerque, New Mexico 87185

P. K. Mast
Science Applications, Incorporated
Albuquerque, New Mexico 87102

F. Briscoe
United Kingdom Atomic Energy Authority
Safety and Reliability Directorate
Culcheth, England

October 1983

Sandia National Laboratories
Albuquerque, New Mexico 87185
Operated by
Sandia Corporation
for the
U.S. Department of Energy

Prepared for the
U.S. Nuclear Regulatory Commission
Washington, D.C. 20555
NRC FIN A1016

* This work was supported by the U.S. Nuclear Regulatory Commission and the United Kingdom Atomic Energy Authority and performed at Sandia National Laboratories which is operated for the U.S. Department of Energy under contract number DE-AC04-76DP00789.

** Now at Electric Power Research Institute, Palo Alto, California.

ABSTRACT

This topical report presents the preliminary results and analysis of the High Ramp Rate fuel-disruption experiment series. These experiments were performed in the Annular Core Research Reactor at Sandia National Laboratories to investigate the timing and mode of fuel disruption during the prompt-burst phase of a loss-of-flow accident. High-speed cinematography was used to observe the timing and mode of the fuel disruption in a stack of five fuel pellets. Of the four experiments discussed, one used fresh mixed-oxide fuel, and three used irradiated mixed-oxide fuel.

Analysis of the experiments indicates that in all cases, the observed disruption occurred well before fuel-vapor pressure was high enough to cause the disruption. The disruption appeared as a rapid spray-like expansion and occurred near the onset of fuel melting in the irradiated-fuel experiments and near the time of complete fuel melting in the fresh-fuel experiment. This early occurrence of fuel disruption is significant because it can potentially lower the work-energy release resulting from a prompt-burst disassembly accident.

CONTENTS

| | <u>Page</u> |
|---|-------------|
| ABSTRACT | iii |
| ACKNOWLEDGMENT | ix |
| 1. INTRODUCTION AND SUMMARY | 1-1 |
| 2. BACKGROUND | 2-1 |
| 3. HRR EXPERIMENT MATRIX AND FUEL CHARACTERIZATION | 3-1 |
| 3.1 Scoping Calculations | 3-1 |
| 3.2 Fuels Characterization | 3-6 |
| 4. EXPERIMENT DESCRIPTION | 4-1 |
| 4.1 Experiment Apparatus and Setup | 4-1 |
| 4.2 Instrumentation | 4-1 |
| 4.3 Reactor Coupling Factor and Shape Function | 4-7 |
| 5. EXPERIMENT RESULTS AND PRELIMINARY ANALYSIS | 5-1 |
| 5.1 Summary of HRR Transients | 5-1 |
| 5.2 Thermal Analysis | 5-8 |
| 5.2.1 Analysis of fresh-fuel experiment HRR-6 | 5-12 |
| 5.2.2 Analysis of irradiated-fuel experiments HRR-2,-3,-5 | 5-22 |
| 5.2.3 Comparisons between fresh- and irradiated-fuel experiments | 5-37 |
| 5.3 Postexperiment Fission-Gas Calculations | 5-40 |
| 6. SUMMARY AND CONCLUSIONS | 6-1 |
| REFERENCES | R-1 |
| APPENDIX A - ASSUMED FUEL FISSION-GAS DISTRIBUTION | A-1 |
| DISTRIBUTION | D-1 |

LIST OF FIGURES

| <u>Figure</u> | | <u>Page</u> |
|---------------|--|-------------|
| 3-1 | Idealized temperature history of High-Ramp-Rate (HRR) experiments. | 3-3 |
| 3-2 | TIGRS calculations of crack propagation. | 3-4 |
| 4-1 | Fuel-disruption-experiment package. | 4-2 |
| 4-2 | Fuel-pin image as seen by camera. | 4-3 |
| 4-3 | Photographs of FD inner canister and disrupting fuel pin. | 4-4 |
| 4-4 | Placement of FD capsule in ACRR. | 4-5 |
| 4-5 | Axial-energy-deposition profile calculated by TWOTRAN-II: HRR series. | 4-9 |
| 4-6 | Typical radial-energy-deposition profile calculated by TWOTRAN-II (HRR-5 shown). | 4-10 |
| 5-1 | ACRR power history for HRR-6. | 5-2 |
| 5-2 | ACRR power history for HRR-2. | 5-3 |
| 5-3 | ACRR power history for HRR-3. | 5-4 |
| 5-4 | ACRR power history for HRR-5. | 5-5 |
| 5-5 | Geometry modeled in thermal analyses. | 5-9 |
| 5-6 | Geometry for fuel pin and holder. | 5-10 |
| 5-7 | Photos of major events for experiment HRR-6. | 5-13 |
| 5-8 | HRR-6 fuel-surface-temperature history. | 5-14 |
| 5-9 | Effect of coupling-factor uncertainty on HRR-6 fuel-surface temperature. | 5-16 |
| 5-10 | HRR-6 radial-temperature profiles. | 5-17 |
| 5-11 | Fuel-expansion data for HRR-6. | 5-19 |
| 5-12 | HRR-6 pressure-transducer history. | 5-21 |
| 5-13 | HRR-2 fuel-surface-temperature history. | 5-23 |
| 5-14 | HRR-3 fuel-surface-temperature history. | 5-24 |
| 5-15 | HRR-5 fuel-surface-temperature history. | 5-25 |

LIST OF FIGURES (Continued)

| <u>Figure</u> | | <u>Page</u> |
|---------------|--|-------------|
| 5-16 | HRR-2 radial-temperature profiles. | 5-26 |
| 5-17 | HRR-3 radial-temperature profiles. | 5-27 |
| 5-18 | HRR-5 radial-temperature profiles. | 5-28 |
| 5-19 | Selected frames from motion-picture film (HRR-2). | 5-29 |
| 5-20 | Selected frames from motion-picture film (HRR-3). | 5-30 |
| 5-21 | Selected frames from motion-picture film (HRR-5). | 5-31 |
| 5-22 | Fuel-expansion data for HRR-2. | 5-33 |
| 5-23 | Fuel-expansion data for HRR-3. | 5-34 |
| 5-24 | Fuel-expansion data for HRR-5. | 5-35 |
| A-1 | Initial intragranular fission-gas concentration (based on Randklev's work). | A-2 |
| A-2 | Initial intergranular fission-gas concentration (based on Randklev's work). | A-2 |

LIST OF TABLES

| <u>Table</u> | | <u>Page</u> |
|--------------|--|-------------|
| 3-1 | HRR experiment matrix: design parameters | 3-5 |
| 3-2 | Information to be obtained from HRR experiments | 3-5 |
| 3-3 | Summary of fuel characteristics | 3-7 |
| 4-1 | Instrumentation used in HRR experiments | 4-6 |
| 4-2 | ACRR coupling factors for HRR experiments | 4-8 |
| 4-3 | Axial-energy-deposition profile for all HRR experiments | 4-9 |
| 4-4 | Radial-energy-deposition profiles for HRR experiments | 4-10 |
| 5-1 | Summary of event timing in HRR experiments | 5-6 |
| 5-2 | Pin powers and reactor-pulse summary | 5-7 |
| 5-3 | HRR experiment matrix: Key parameters | 5-8 |
| 5-4 | HRR fuel-melt-fraction summary at time of disruption | 5-32 |
| 5-5 | Time of fuel-vapor-pressure generation in HRR experiments | 5-36 |
| 5-6 | Summary of observations for high-ramp-rate fuel-disruption experiments | 5-38 |
| 5-7 | Comparison of measured and predicted fuel-disruption times for experiments HRR-2, -3, and -5 | 5-41 |
| A-1 | Gas concentration summary | A-3 |

ACKNOWLEDGMENTS

The authors gratefully acknowledge Dale Fastle and Richard Padilla for their complete handling of all photographic work required by these experiments. Credit and thanks also go to the personnel of the Hot Cell Facility (especially Ellen Edge) and to the Annular Core Research Reactor operators. Finally, very special thanks go to Dick Toth and Neil Simmons for their careful attention to detail and safety in assembling these experiments.

1. INTRODUCTION AND SUMMARY

Past analysis of hypothetical core-disruptive accidents (HCDAs) involving prompt-critical power excursions shows that the ultimate potential for damage to the reactor vessel is highly dependent on the energy deposited in the fuel during the excursion. Several authors have noted that significant reductions in the work potential can occur if the fission products disperse the fuel near the time of fuel melting, prior to the action of fuel vapor pressure, thereby leading to an earlier termination of the power burst.[1,2] A number of experiments have indicated that this early fuel dispersal may occur.[3] These factors led to the design of a new series of fuel-disruption experiments to investigate this phenomenon in more detail.

A series of six experiments was performed in the Annular Core Research Reactor (ACRR) at Sandia National Laboratories, Albuquerque (SNLA). These "High-Ramp-Rate" (HRR) experiments were cosponsored by the United States Nuclear Regulatory Commission (USNRC) and the United Kingdom Atomic Energy Authority (UKAEA). Their objective was to use high-speed cinematography to investigate the timing and mode of fuel disruption under conditions typical of a prompt-critical excursion in a liquid-metal fast-breeder reactor (LMFBR) following an unprotected loss-of-flow (LOF) accident. In these experiments a stack of five fuel pellets was subjected to a prompt-burst power transient that simulated the conditions of prompt-burst HCDAs. Analysis of the experiments has provided information concerning the state of the fuel at the time of disruption (i.e., solid, substantially molten, or at temperatures of significant fuel-vapor pressure), as well as information concerning the likelihood of early fuel dispersal.

Six experiments were performed in the summer and fall of 1980. This report describes four of these experiments and presents their preliminary results. A brief summary follows.

The power transients for these experiments consisted of a short preheat followed by a rapid temperature ramp. The preheat, lasting about 2.5 s, was designed to simulate the LOF accident sequence prior to the prompt burst. Realistic temperature profiles were achieved, and the cladding was allowed to melt and drain prior to the power burst. Fuel temperatures in the unrestructured fuel zone ($r/R_0 = 0.8$) in the experiments varied between 2100 and 2500 K. Fission-gas redistribution, similar to that expected during the LOF accident, occurred during the preheat phase. This preheat was then followed by a prompt-burst power transient that produced heating rates in the range of 50 to 100 K/ms.

Early scoping fission-gas calculations for these experiments were performed with the TIGRS code.[4] This code calculated transient inter- and intragranular gas release as well as the potential for fuel crack-

ing. These design calculations indicated that the most important parameter for determining the potential for early (solid-state) fuel disruption was the fuel-preheat temperature. Further, it was expected that fuel type (low power, high power, fresh) would affect the disruption potential. A matrix of four experiments was devised to investigate the disruption as a function of preheat temperature and of fuel type. Two experiments had preheat temperatures of 2300 K, and the other pair of experiments had preheat temperatures of 2500 K. Fresh mixed-oxide fuel was used in one experiment, whereas the other three used irradiated mixed-oxide fuel (PNL 11-18 and PNL 9-44). For the irradiated-fuel experiments, the burnup was nearly constant at 4.6 atom percent, but the linear heat rating varied between 16 and 33 kW/m. Only one parameter at a time was varied between experiments.

The analysis of the experiments consisted of thermodynamic and limited fission-gas calculations. The thermodynamic calculations were performed with the SANDPIN code and were used to determine the fuel and clad temperatures, given the measured reactor power.[5] Significant events recorded by the film (swelling, fuel disruption, and gas release) were then correlated with the fuel temperature to help identify phenomena that may have been responsible for the observed fuel behavior. The early-design fission-gas calculations were performed with the TIGRS code, as mentioned above. Posttest fission-gas calculations were performed using the SANDPIN code, which is largely based on the TIGRS formalism but has a more sophisticated treatment of intergranular fission gas.

Analysis of the films and thermodynamic calculations were used to determine the mode of fuel disruption and the state of the fuel at the time of disruption. Qualitatively, the disruption that occurred in each of the four experiments was much the same in each case, with rapid, spray-like expansion occurring well into the prompt burst that followed the preheat. The thermal analyses showed that, in all cases, the fuel disruption occurred significantly prior to fuel-vapor-pressure generation, near the time of fuel melting. For the irradiated fuel, no significant differences in the mode or timing of disruption could be attributed to the preheat temperature or to the fuel type. However, significant differences in timing and character of disruption existed between fresh and irradiated fuel.

In the fresh-fuel experiment (mixed-oxide fuel), the disruption started as a rapid fuel swelling when the fuel-surface temperatures reached 2700 to 2800 K. Swelling continued until the onset of disruption, at which time the change in volume due to swelling had reached 20 to 30%, and the areal melt fraction (area of fuel with temperatures greater than the solidus temperature) was nearly 100%. No swelling of this type was seen in any of the irradiated-fuel experiments. However, in the irradiated experiments, the disruption occurred earlier and was more energetic. The melt fractions in those cases varied from 0 to 44%. Considering the uncertainties in this calculated melt fraction, it may be concluded that in these experiments the onset of fuel disruption coincides with the onset of fuel melting. Analysis of the transient fission-gas behavior suggests that solid-state disruption of the irradiated fuel may have occurred.

However, at this time, the center of the fuel pin was already starting to melt.

Based on these observations and the preliminary thermal and fission-gas analyses done to date, the following interpretations have been made concerning the cause of the disruption:

- The most likely causes of the observed early fuel disruption (i.e., prior to fuel-vapor-pressure generation) in the fresh-fuel experiment are impurity gases (possibly impurities left in the fuel at the time of fabrication), augmented by the volume expansion upon fuel melting.
- For the irradiated fuel, the most likely causes for early fuel disruption are fission products, augmented by impurity gases and volume expansion upon melting.

These observations -- if they can be generalized to actual reactor accident transients -- provide promise for early termination of reactor disassemblies. However, it must still be demonstrated that the mode of disruption observed here, when coupled with rapid coolant-vapor streaming, yields the negative reactivity feedback needed to terminate the accident excursion. Thus, it must still be shown that the early fuel breakup seen in these experiments leads to rapid axial fuel dispersal in a prototypic bundle geometry. Experiment programs designed to investigate this axial dispersal are currently underway at SNLA. These experiments are similar to the fuel-disruption-type experiments but use single-pin and multi-pin bundles in a flowing gas-cooled environment.

2. BACKGROUND

Since the inception of fast-reactor safety analyses, considerable attention has been focused on HCDAs involving prompt-critical power excursions. Such prompt-critical excursions are a possible outcome of many LMFBR accident initiators (e.g., loss of flow, transient overpower, structural failure) and may, under worst conditions, represent a direct threat to the integrity of the primary containment through the mechanical energy released.[6] This mechanical energy can come directly from the expansion of the hot core materials (fuel, cladding), from the expansion of the surrounding sodium following heat transfer from hot core materials to the sodium, or from a missile generated by rapid momentum transfer from fuel to upper internal structures. In all three cases, the ultimate work potential (and hence damage to the containment) is closely tied to the magnitude of the thermal energy released during the power excursion.

The first attempt to estimate nuclear-excursion yields in HCDAs assumed that the excursion would be terminated only by core disassembly resulting from high fuel-vapor pressure.[7] Many improvements were made to this type of analysis (such as the modeling of Doppler reactivity feedback), which had the effects of slowing down the estimated rate of power increase and hence of predicting disassembly at lower energy deposition. However, the ultimate mechanism for disassembly remained fuel-vapor pressure.[8]

More recently, it has been suggested that the large quantities of fission products present even in low-burnup cores represent a dispersive potential that could lead to the beginning of core disassembly at much lower energy densities (near the time of fuel melting rather than fuel boiling) and so further reduce the nuclear-excursion yield.[9] This dispersive potential was explored in several sensitivity studies that showed that up to an order of magnitude decrease in the nuclear excursion yield could be realized under some conditions (depending on fission gas characterization, Doppler coefficient, and imposed reactivity ramp rates).[1,2] Later studies, however, indicated that this reduction might not be realized for all accident scenarios. For example, in a transient overpower (TOP) accident the radial fuel-temperature profile interacts unfavorably with the radial distribution of retained fission gas. When fission-gas pressure is significant near the outer part of the fuel pin, fuel-vapor pressure is already significant at the pin center.[10]

Most of the sensitivity studies referred to above used rough estimates of the quantity of gas remaining in the fuel at the time of the prompt-critical excursion, assumed that this gas became available to pressurize the fuel at the time of fuel melting (or with an arbitrary time delay after fuel melting), and assumed that fission-gas pressure

acted in the same manner as fuel-vapor pressure to disperse the fuel. To quantify and justify these estimates and assumptions, several uncertainties need to be addressed. These include

- The quantity and characterization (inter- versus intragranular, bubble-size distribution, impurities) of the fission products at the start of the prompt burst (as a function of the release and redistribution during the initiating phase of the accident)
- The timing of fission-gas pressurization during the prompt burst, i.e., the gas-bubble dynamics (fission-gas temperature versus fuel temperature and degree of overpressure in gas bubbles)
- The mode of fuel dispersal, i.e., does the fuel disperse in the molten state as a froth in which the fission-gas pressure acts in a manner similar to fuel-vapor pressure, or does the fuel disperse (earlier) in the solid state as a dust cloud in which the dispersive potential of the gas might be less effective

Several experimental and theoretical studies have contributed towards a better understanding of fission-product behavior during the initiating phase of the accident. Some of the important modeling efforts include the FRAS[11] and GRASS[12] codes at Argonne National Laboratory (ANL), the FISSGAS[13] code at SNLA, work done at the University of California at Los Angeles[14], and work done at Harwell.[15] Early efforts in this area concentrated on intragranular bubble dynamics and the associated swelling and gas release. However, attempts at comparing model predictions to experiment results demonstrated the importance of including intergranular bubble dynamics in the models.[16] More recently, the effect of retained fission gas bubbles on possible fuel fragmentation during transients has been investigated at ANL[17] and at SNLA.[4] The SNLA effort led to the development of the TIGRS fission-gas code, which models intra- and intergranular gas dynamics as well as fission-gas-induced fuel fragmentation. Results of calculations using this code are an important part of the work discussed herein.

Two significant experimental programs that provided much of the early data on fission-gas release and swelling during thermal transients were the "Direct Electrical Heating" (DEH) and "Fission-Gas Release" (FGR) experiments.[18,19] In both cases, heating of short fuel-pin segments was performed out-of-pile using direct ohmic heating in the DEH program and external heating in the FGR program. Although these programs provided valuable data on fission-gas behavior for validating fission-gas models under development, they have not to date considered thermal transients in the prompt-burst regime.[20]

Three experiments have been conducted in the Transient Reactor Test facility (TREAT), in which irradiated fuel pins were subjected to "loss of flow driven by transient overpower" (LOF-d-TOP)-type heating conditions. The L6 and L7 experiments simulated LOF-d-TOP power histories in which a power ramp was initiated following coolant voiding. In the L8 experiment, the power burst was initiated prior to coolant voiding.

Fuel-motion diagnostics were provided by the TREAT neutron hodoscope in each case. The results from these three experiments are not conclusive because of the difficulty in interpreting the hodoscope data. Early analysis of the experiments suggested that fuel dispersal occurred shortly after fuel melting (well before significant fuel vapor pressures were generated).[21] However, more recent, careful analysis of this data indicates that for the L7 experiment, fuel dispersal actually occurred somewhat later, near the time when fuel-vapor pressure may have been significant.[22] Thus, while these experiments have demonstrated some potential for early fuel dispersal, they have not provided the quantitative data needed to develop models to treat these phenomena.

The VIPER series of experiments, conducted at the United Kingdom's Atomic Energy Research Establishment (AERE), has attempted to provide more phenomenological data on fission-gas pressurization and fuel movement in irradiated fuel samples subjected to fast heating rates (with no preheat).[23] So far, however, the analysis of these experiments has been hampered by the presence in the fuel samples of contaminant gases in addition to the fission gases. This raises the question of whether inherent contaminants in reactor fuel could act in the same manner as fission products.

Finally, one experiment in the first series of fuel-disruption experiments (FD 1.6), conducted in the ACRR at SNLA, was performed under prompt-burst heating conditions.[24] A detailed analysis of this experiment showed that the preirradiated test fuel disrupted significantly prior to fuel-vapor-pressure generation and probably disrupted near (and possibly prior to) the time of fuel melting.[3] This analysis suggested that fission products were indeed responsible for the observed early disruption. However, in this experiment, the cladding was still on the fuel at the time of disruption. Thus, fuel-surface-temperature measurements were not available to use as a check on the accuracy of the thermal analysis performed.

To investigate this question of fission-gas-induced fuel dispersal under rapid heating conditions in more detail, a series of six fuel-disruption experiments was conducted in the ACRR facility at SNLA. These experiments, called the "High Ramp Rate" (HRR) series, were sponsored jointly by the USNRC and the UKAEA. The objective of these experiments was to use high-speed cinematography to determine visually the timing and mode (swelling, solid-state breakup, rapid gas-driven expansion, etc.) of fuel disruption and the state of the fuel at the time of disruption during simulated loss-of-flow-induced prompt-burst disassembly transients. Analysis of the experiments could then provide insight into the timing and likelihood of early fuel dispersal, either in the solid state or shortly after melting.

The HRR experiments were performed in the summer and fall of 1980. This report describes four of the six experiments performed and presents a preliminary analysis of the results. It is the intention of this report to present enough of the experimental conditions and analysis to allow other investigators to undertake their own analysis and interpretation of the results. Further analysis is also continuing at SNLA.

3. HRR EXPERIMENT MATRIX AND FUEL CHARACTERIZATION

Theoretical work on fission-gas behavior indicates the possibility of fission-gas-driven fuel disruption not only in the liquid state but also when the fuel is still solid. Such solid-state disruption is probably more difficult to achieve than liquid-state disruption. For this reason, the HRR transients were optimized to maximize the likelihood of solid-state disruption while still maintaining the basic experiment objective of simulating LOF-d-TOP conditions. Scoping calculations of fission-gas effects were used to achieve these design objectives as well as to select the major parameters of the experiment matrix.

In addition to the scoping calculations, this chapter also describes the major characteristics of the fuel used in the four experiments.

3.1 Scoping Calculations

The definition of the HRR experiment matrix (power histories, fuel used) was motivated by the results and analysis of the FD 1.6 experiment. Posttest thermal analysis of that particular experiment indicated that the observed vigorous fuel dispersal occurred while the fuel sample was near the melting temperature and possibly in the solid state.[3] This result, therefore, suggested that fission products were responsible for the observed disruption, and led to the development of the TIGRS model of intra- and intergranular fission-gas behavior during transient heating conditions.[4]

The TIGRS code models the intra- and intergranular gas bubble dynamics (swelling and gas release) as well as the potential for fuel cracking. The fuel-cracking potential is evaluated using five crack-propagation criteria that deal with the interlinkage of intra- and intergranular bubbles. It should be noted that, when complete cracking is calculated in TIGRS, this does not necessarily represent fuel disruption. Solid-state disruption requires not only severe cracking of the fuel, but also sufficient excess energy to disperse the fuel. This latter dispersion is not modeled in the TIGRS code.

Using the TIGRS code with a suitable choice of model parameters, it was possible to show that the five crack-propagation criteria in TIGRS were indeed satisfied for the FD 1.6 transient near the observed time of fuel disruption. Based on this apparent positive result, it was decided to investigate further the likelihood of solid-state fuel disruption and to define the HRR power transients to maximize that likelihood.

Scoping calculations were performed using an updated version of the TIGRS code. These scoping calculations were carried out for a hypothetical heating transient that was assumed to provide an idealized

fuel-temperature history as shown in Figure 3-1. This temperature history included an initial linear heatup lasting until $t_1 = 0.25$ to 0.50 s, a period at constant temperature $T_s = 2000$ to 2700 K lasting for $\Delta t = 2.0$ to 2.5 s, and a final linear heatup at rates $\dot{T} = 50$ to 150 K/ms.

The scoping calculations were performed for a single "gassy" fuel node from the unrestructured fuel region, assuming a constant radial-temperature gradient of 1×10^5 K/m. An important parameter in these analyses was the concentration and distribution (inter- versus intragranular) of fission gas at the start of the transient. The calculations were performed for PNL 11-18 fuel, which was used in the test matrix. Best-estimate calculations used fission-gas distributions as described in Section 4.2 and Appendix A. For the PNL 11-18 fuel pin, these distributions predicted initial peak gas concentrations of 1.5×10^{26} atoms/m³ intragranular and 3.7×10^{25} atoms/m³ intergranular. However, because of the large uncertainties in these gas concentrations, the scoping calculations were also repeated assuming a gas concentration of $1.33 \times$ nominal. Using this assumption, the calculated peak intragranular gas concentration was 2.0×10^{26} atoms/m³. This latter assumption is more consistent with the earlier FD 1.6 calculations.[3]

Several general results were immediately obtained. Because most of the physical processes in the TIGRS model have an exponential dependence on temperature, the preheat temperature was calculated to be much more important than the length of the preheat. Therefore, the length of the preheat was chosen to be long enough (> 2 s) to ensure that cladding melting would precede the initiation of the fast heating transient. Thus, the visual diagnostics were assured of observing the fuel behavior during disruption.

For the range of preheat temperatures and temperature-ramp rates investigated, the results were strongly dependent on the initial gas concentration. In no case were the five crack-propagation criteria satisfied when the best-estimate fission-gas concentrations were used. However, the same criteria were satisfied in several of the cases analyzed when the $\sim 33\%$ higher concentration was assumed. To determine more clearly the effects of the transient temperature history on the likelihood of solid-state disruption, subsequent scoping calculations were always performed using these higher concentrations.

Another general observation was that the TIGRS predictions of crack interlinkage were insensitive to the magnitude of the final temperature ramp, for heating rates in the range of 50 to 150 K/ms. Therefore, for subsequent scoping calculations, the final temperature ramp was set at 100 K/ms.

The preheat temperature was, therefore, selected as the major parameter of the scoping calculations. It was varied from 2000 to 2600 K, but the preheat time was fixed at 2.35 s. Figure 3-2 shows that the potential for crack propagation increases with preheat temperature up

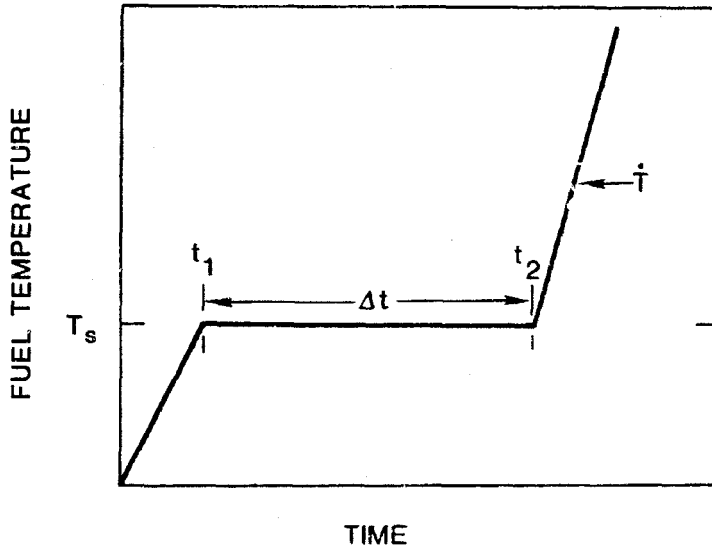


Figure 3-1 Idealized temperature history of High-Ramp-Rate (HRR) experiments.

to about 2500 K. At low preheat temperatures (< 2100 K), intragranular fission-gas-bubble migration to the grain boundaries and coalescence of the bubbles on the grain boundary does not occur fast enough to generate sufficiently high pressures to cause crack propagation. At high preheat temperatures (> 2500 K), power-law creep intervenes to equilibrate fission-gas bubbles and so prevent crack propagation. For the heating transients in which the five crack-propagation criteria are satisfied, the last criterion to be satisfied is always the total-energy criterion. Thus, TIGRS predictions of the potential for crack propagation are most sensitive to the model parameters that govern the total-energy criterion (such as the crack-opening displacement). In all cases, cracking was calculated to occur on the grain boundaries.

Based on these results, the HRR power histories were designed to achieve preheat temperatures in the ranges of 2100 to 2500 K. A matrix of four experiments was planned, varying only the preheat temperature and fuel type. With this particular matrix, shown in Table 3-1, several direct comparisons of experimental results are possible. These comparisons are summarized in Table 3-2.

For the HRR-6 versus HRR-2 comparison, the motivation is obvious: the presence of fission gas in the irradiated HRR-2 fuel sample but not in the fresh HRR-6 fuel sample. The expected result is that the fuel will disrupt earlier (either solid or liquid state) in the HRR-2 test. The HRR-2 versus HRR-3 comparison investigates the results of the

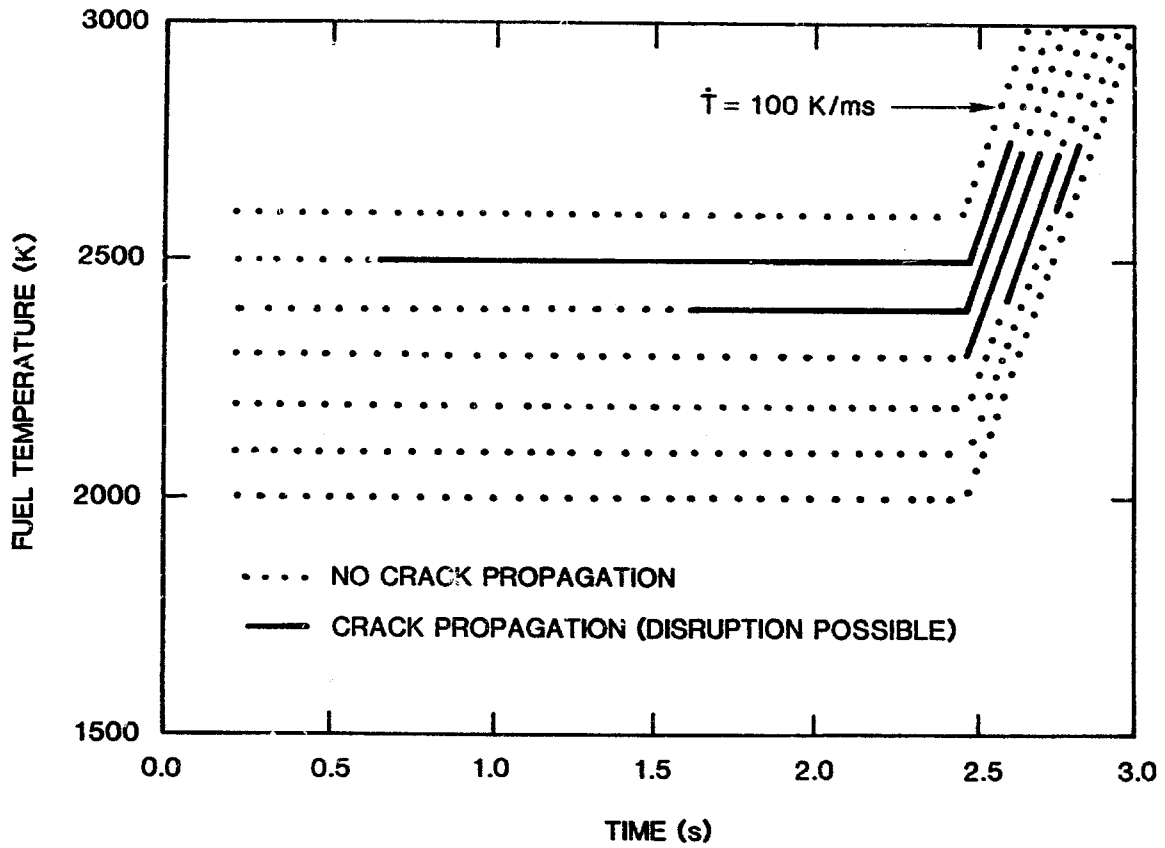


Figure 3-2 WIGRS calculations of crack propagation.

Table 3-1 HRR experiment matrix: design parameters

| Experiment Designation* | Fuel Characterization | | | Preheat Temperature (K) | Preheat Time (s) | Temperature Ramp (K/ms) |
|-------------------------|--------------------------|------------|----------------------------|-------------------------|------------------|-------------------------|
| | Pin | Burnup (%) | Linear Heating Rate (kW/m) | | | |
| HRR-6 | (Fresh mixed-oxide fuel) | | | 2300 | ~ 2.5 | ~ 100 |
| HRR-2 | PNL 11-18 | 4.67 | 33.3 | 2300 | ~ 2.5 | ~ 100 |
| HRR-3 | PNL 11-18 | 4.61 | 32.9 | 2500 | ~ 2.5 | ~ 100 |
| HRR-5 | PNL 9-44 | 4.75 | 15.9 | 2500 | ~ 2.5 | ~ 100 |

* Experiments HRR-1 and HRR-4 are not included because of instrumentation failure.

Table 3-2 Information to be obtained from HRR experiments

| Comparison | Direct Information Obtained |
|-----------------|---|
| HRR-6 vs. HRR-2 | Difference in behavior between fresh and preirradiated mixed-oxide fuel subjected to the same power history |
| HRR-2 vs. HRR-3 | Difference in behavior for same fuel type (burnup, linear heat rate) for similar transients with different preheat temperatures |
| HRR-3 vs. HRR-5 | Difference in behavior between fuels of different microstructure (linear heat rate) for same burnup and same power history |

TIGRS scoping calculations. These calculations suggest that early disruption in the solid state is more likely in the HRR-3 transient because of the higher preheat temperature. The final comparison between HRR-3 and HRR-5 investigates the effect of microstructure and possibly total initial gas content.

3.2 Fuels Characterization

As mentioned in the previous section, the four HRR experiments used fuel samples from a PNL 11-18 pin, a PNL 9-44 pin, and fresh mixed-oxide pellets. The major characteristics of these fuel types are summarized in Table 3-3. Approximately 5.5 g of (~ 90% theoretical density) mixed-oxide fuel was used in all experiments. For the irradiated samples, these pin sections came from near the center of the

EBR-II pins indicated. The burnup and linear heat rating, obtained from the Hanford Engineering Development Laboratory's irradiation history report, correspond to the local values for the sample.[25-27] The burnup was nearly the same, 4.7 atom percent, for all three samples. However, the fuel enrichment ranged from 40 to 70%, and the linear heat rating ranged from 16 to 33 kW/m.

Detailed analysis of sibling pins (in this case, pellets directly adjacent to the samples) has not yet been performed. Thus, analysis of the experiments was based on the fuel microstructure characterization as obtained from the steady-state fuel performance code SIEX.[28] Errors in this assumed microstructure characterization could have a significant effect on the calculated cladding temperature (because of uncertainties in the fuel-cladding gap size).

Of considerable importance for the analysis is the retained fission-gas distribution in the fuel samples. The gas content as obtained from the SIEX code is based on the use of the Dutt correlation.[29] However, recent experimental work by Randklev[30,31] and by Bandyopadhyay[32] has shown that neither the total (integrated over fuel radius) gas content nor the radial distribution is described very well by the Dutt correlation. This lack of agreement with the Dutt correlation is also seen in the results of theoretical descriptions of steady-state gas release.[33] Unfortunately, results on measured gas concentrations published to date have been very qualitative, with large uncertainties in the absolute gas-concentration values.

The retained-fission-gas-concentration values shown in Table 3-3 are based on an analysis of work published by Randklev.[30,31] For comparison, the concentrations as predicted by the Dutt correlation are also included in Table 3-3. A detailed summary of the assumed gas-concentration distribution is given in Appendix A. Uncertainties, especially in the peak concentrations, arise from uncertainties in the total amount of retained gas, fractional split between inter- and intragranular gas, and the assumed inter- and intragranular distributions. Recognizing the resulting large uncertainties in peak gas-concentration values, the scoping calculations and best-estimate calculations were also performed assuming an uncertainty of $\pm 30\%$ in gas content.

Table 3-3 Summary of fuel characteristics

| | HRR-6 | HRR-2 | HRR-3 | HRR-5 |
|--|--------|-----------|-----------|----------|
| <u>Fabrication Parameters</u> | | | | |
| Fuel Type | FE-094 | PNL 11-18 | PNL 11-18 | PNL 9-44 |
| Enrichment (%) | 70.3 | 67.2 | 67.2 | 40.0 |
| Sintered Density (10^3 kg/m ³) | 10.01 | 9.96 | 9.96 | 9.88 |
| <u>Results of EBR-II Irradiation*</u> | | | | |
| Linear Heat Rating (kW/m) | -- | 33.3 | 32.9 | 15.9 |
| Burnup (atom percent) | 0.0 | 4.67 | 4.61 | 4.75 |
| <u>Fuel Microstructure[†]</u> | | | | |
| Center Void (mm) | -- | 0.6 | 0.6 | 0.0 |
| Columnar Radius (mm) | -- | 1.8 | 1.8 | 0.0 |
| Equiaxed Radius (mm) | -- | 1.94 | 1.94 | 1.4 |
| Fuel/Clad Gap (μ m) | 70 | 13.5 | 13.5 | 37.0 |
| Inner Cladding Radius (mm) | 2.54 | 2.54 | 2.54 | 2.54 |
| Cladding Thickness (mm) | 0.381 | 0.381 | 0.381 | 0.381 |
| <u>Gas Content[‡]</u> | | | | |
| Peak intragranular (10^{25} atoms/m ³) | -- | 15.0 | 15.0 | 14.6 |
| Peak intergranular (10^{25} atoms/m ³) | -- | 3.70 | 3.70 | 3.60 |
| Dutt correlation (10^{25} atoms/m ³) | -- | 14.7 | 14.7 | 15.5 |

* Average values for sample used.

† Room temperature values.

‡ See Appendix A for description of radial distributions.

4. EXPERIMENT DESCRIPTION

4.1 Experiment Apparatus and Setup

The experiment package consisted of three major sections (see Figure 4-1). The first section consisted of the inner canister and contains the fuel, its mounting bracket, and an assortment of lights, mirrors, and prisms that transmitted the fuel-pin image through a quartz window in the top of the canister. The inner canister also served as the primary containment vessel. The second section consisted of a large cylindrical canister that contained the inner canister and some instrumentation. It also had a quartz window at the top. The third or top section consisted of a borated polyethylene ("poly") annulus. It served as a partial neutron shield to reduce the dose delivered to the reactor operating staff and the experimenters.

The experiment package transmitted a split image of the front and back portions of the fuel pin section to the camera. Figure 4-2 illustrates the split image. Note that "down" is always towards the center of the image. Prior to significant fuel heating, the fuel pin was backlighted; however, after the cladding had melted off, the fuel glowed brighter than the backlight. Photographs of the inner experiment canister and a typical view of a test-pin section are shown in Figure 4-3.

Figure 4-4 shows how the fuel-pin image was transmitted out of the experiment package through the experiment tube (~ 10 m) and then reflected off a large mirror to a Celestron telescope and high-speed camera.

Approximately 5.5 g of fuel was used in each experiment. The fuel consisted of five fuel pellets clad in 20% cold-worked 316 stainless steel. The irradiated-fuel experiments used three irradiated mixed-oxide fuel pellets mounted between two fresh UO₂ pellets of the same enrichment. The fresh-fuel experiment used five fresh mixed-oxide fuel pellets. The fuel was held in place by a spring-loading mechanism, which placed a 56-g load on the fuel pellet stack. This simulated the weight of a 254-mm fuel stack resting on top of the pellets.

4.2 Instrumentation

A high-speed camera and the reactor-power monitors were the major diagnostic tools. Other types of instrumentation provided fuel- and cladding-surface-temperature and gas-pressure measurements. Table 4-1 lists the various diagnostic devices and gives some important characteristics of each device. A brief description of each device follows.

A Hi-cam camera recorded the disruption process. This camera viewed the fuel-pin section through a 200-mm-diameter Celestron telescope at

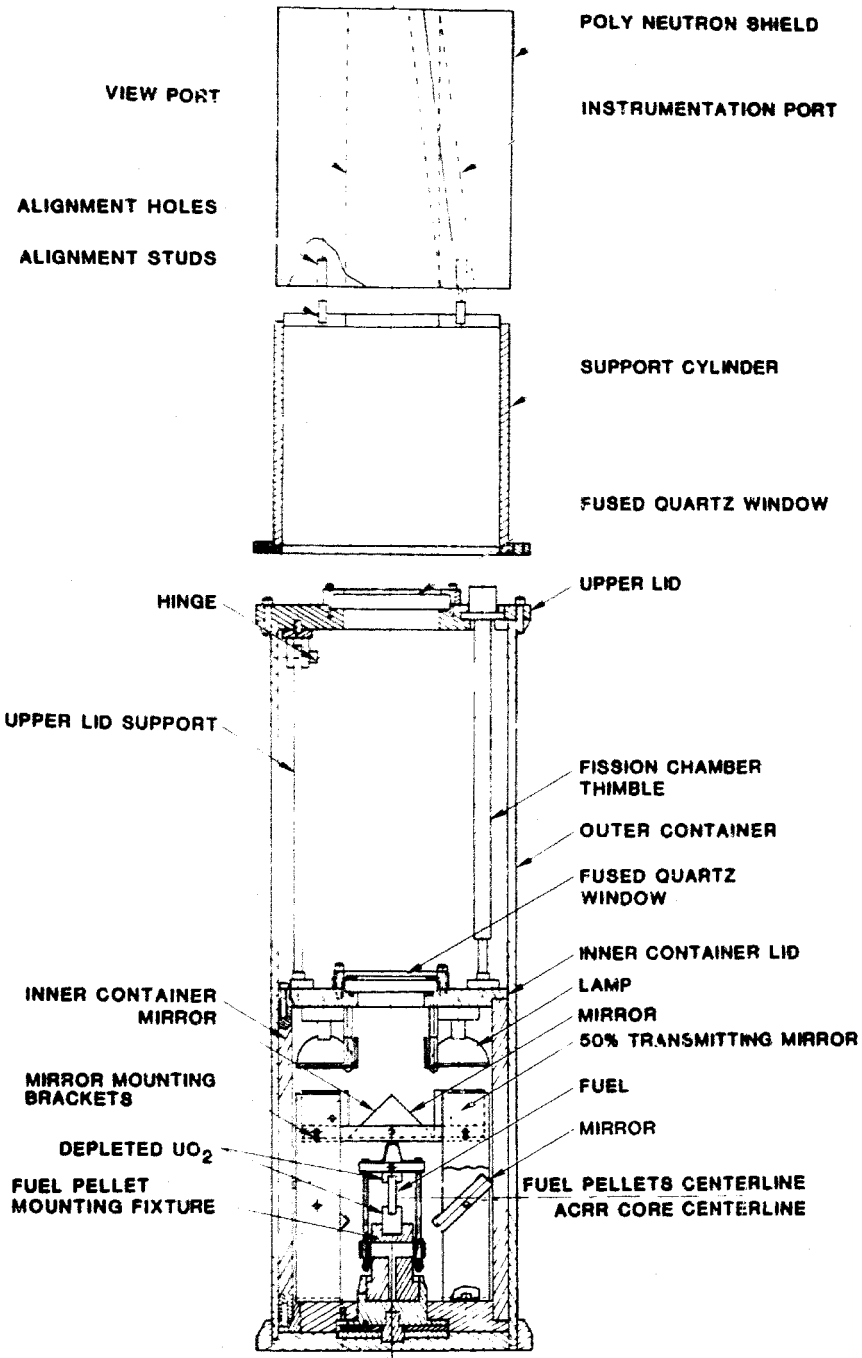


Figure 4-1 Fuel-disruption-experiment package.

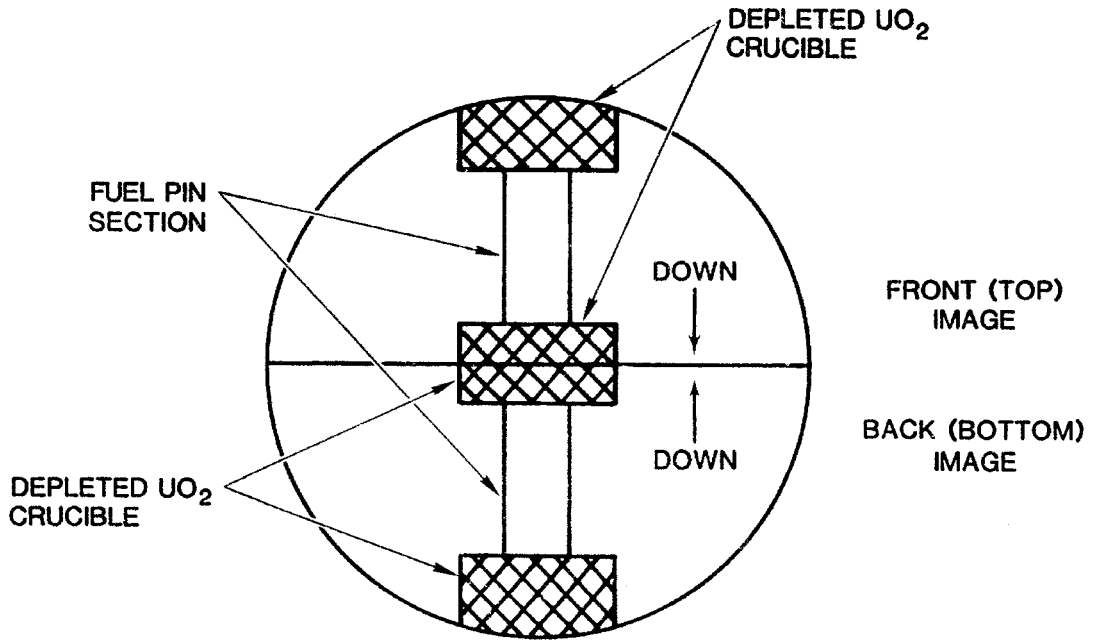
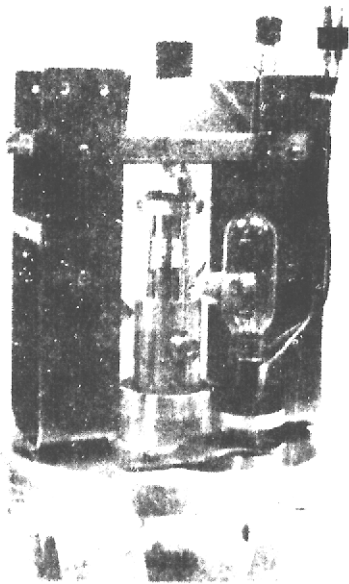
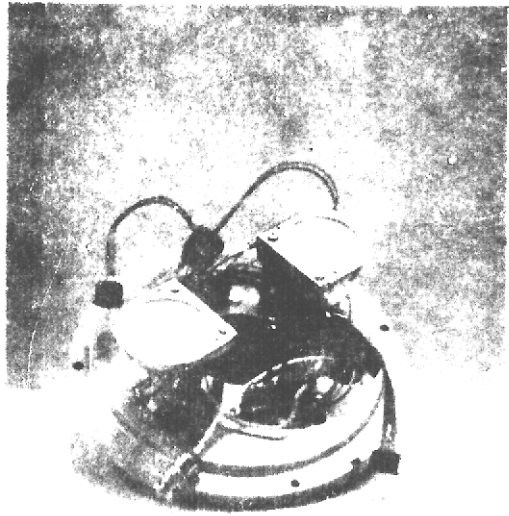


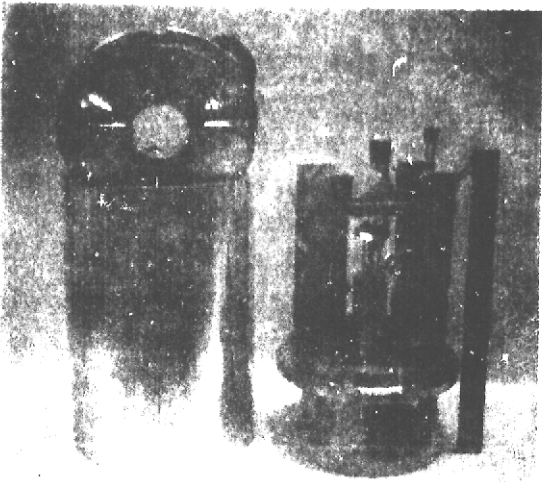
Figure 4-2 Fuel-pin image as seen by camera.



a. Fuel-pin assembly and optics.



b. Lid, quartz window, and lamps.



c. Complete inner canister.



d. Fuel pin prior to disruption.

Figure 4-3 Photographs of FD inner canister and disrupting fuel pin

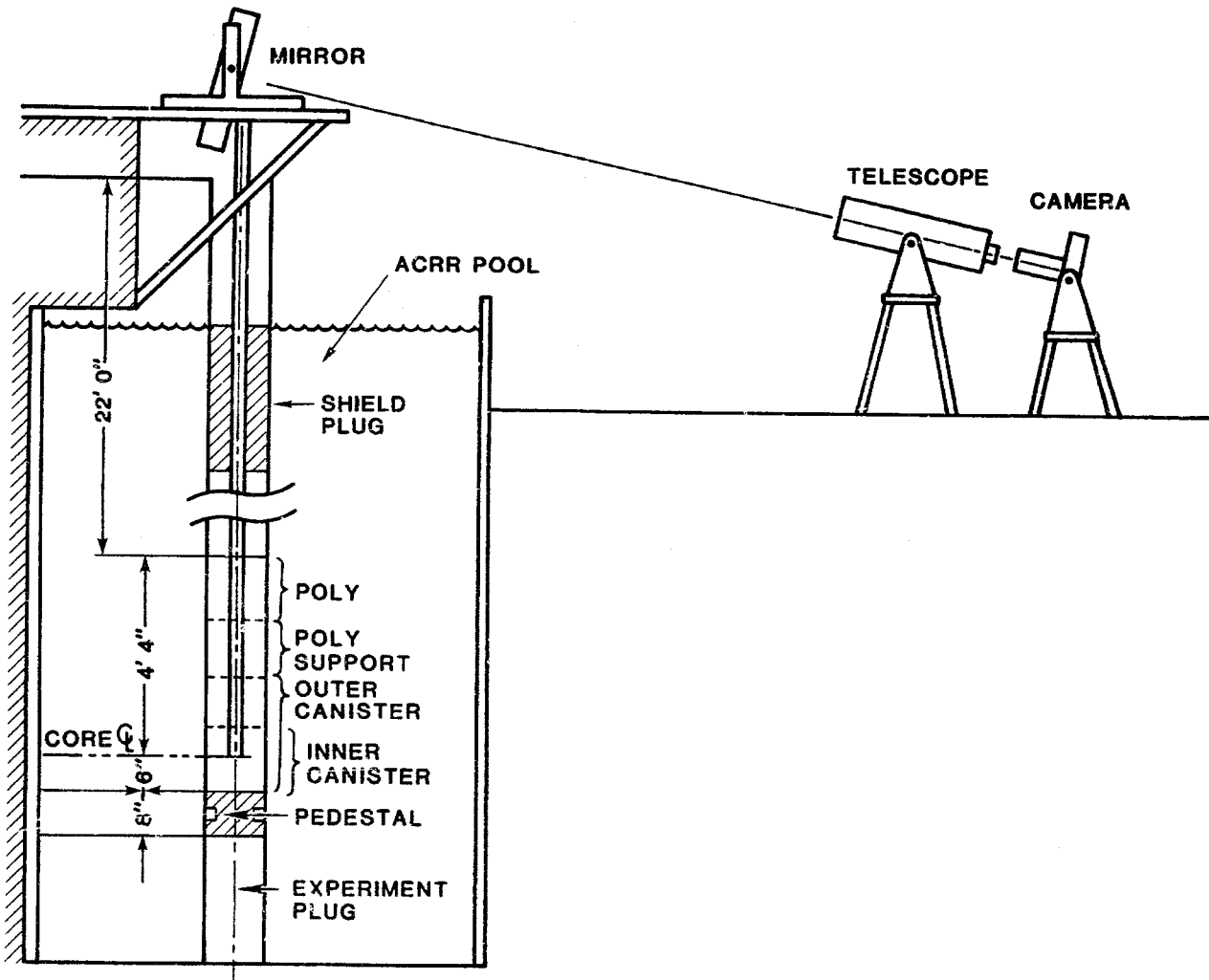


Figure 4-4 Placement of FD capsule in ACRR.

Table 4-1 Instrumentation used in HRR experiments

| Detector | Location | Measurement and Range | Time Response |
|---------------------------------------|--------------------|---|---------------|
| High-speed camera "Hi-Cam" | Reactor room floor | 200 to 10 000 frames per second | -- |
| Cadmium self-powered neutron detector | Reactor core | 0 to 40 000 MW (reactor power) | 1 μ s |
| Fission chamber* (reactor power) | Outer canister | 0 to 40 000 MW | 1 μ s |
| Optical pyrometer* "Pritchard" | Reactor room floor | 2000 to 3500 K fuel-surface temperature | 1 ms |
| Pressure transducer "Validyne AP-15" | Inner canister | 0 to 3×10^5 Pa (fuel-vapor pressure) | 1 ms |
| Thermocouple* (W-Re) | Cladding | 0 to 1700 K (clad temp.) | 500 ms |

* HRR-6 experiment only.

a distance of approximately 16 m. The image was filtered through a #25 gelatin Kodak filter and recorded on Kodak XR ASA 400 black-and-white film. For the HRR experiments, the filming rates were varied between 4000 and 10 000 frames per second.

A cadmium self-powered neutron detector (Cd-SPD) measured the reactor power. This detector was located next to the experiment cavity just inside the reactor core. It had a length of 300 mm and a time response of 1 μ s. The output of the detector was a current proportional to the neutron flux over the length of the detector.

A fission chamber was used in experiment HRR-6 to measure the fission rate at or very near the fuel-pin section. A check was made of the proportionality between the Cd-SPD and the fission chamber. No significant differences were observed. The fission chamber used a 30-volt power supply and produced a current output proportional to the fission rate within the detector.

Both the Cd-SPD and the fission chamber were used with reactor coupling factors and energy-deposition shape functions to determine the local energy deposition in the fuel pin (see Section 4.3).

A Validyne AP-15 pressure transducer measured the inner-canister gas pressure. Because of the large volume of the canister (6.3 liters), it is felt that the transducer responded primarily to fuel-vapor pressure.

Two methods were used to determine the fuel surface temperature. In the first method, optical-densitometer measurements of the film exposure were made to determine the fuel radiance in a narrow band of wavelengths around 0.63 μm . The surface temperature could then be determined using single-color optical-pyrometry techniques.[34] The uncertainties were on the order of ± 100 K. This photographic technique was used in all experiments.

In the second method, an optical pyrometer viewed the fuel pellet stack through a telescope. This device was a modified Pritchard telephotometer, 1970-A, which measured the fuel radiance with an S-11 photomultiplier tube. Again, single-color pyrometry techniques were used to determine the surface temperature. Temperatures between 2000 and 3500 K could be measured with a 1-ms time response. The apparent precision varied from ± 100 K at the lower temperatures to ± 25 K at temperatures above 3000 K.

A tungsten-rhenium thermocouple measured the cladding temperature in the fresh-fuel experiment. The time response of the thermocouple and its amplifier was 0.5 s.

A Data Acquisition and Display System (DADS) recorded the data from each of the these devices. This system used an HP-9845 mini-computer coupled to an analog-to-digital converter and an HP-1000 computer. The system provided quick retrieval of information, plotted all recorded signals, converted all measured signals to physical units, transferred the data to other computer systems, and provided long-term storage of the measured data.

4.3 Reactor Coupling Factor and Shape Function

The reactor coupling factor is defined as the ratio of the average energy density of the test pin to the total energy in the reactor core. Its units are J/g or J/cm³ (in the test pin) per MJ (in the reactor). An accurate knowledge of these ratios is needed to determine the desired reactor pulse shape and to perform posttest analysis. In addition, the axial and radial shape functions of the energy deposition are needed. This section describes the coupling factor and the shape functions used for the HRR experiments.

Both experimental and computational results were used to determine the reactor coupling factor and shape functions. The average energy deposition in a fuel sample was determined using fission-product counting techniques. These results were then used in normalized two-dimensional neutron transport calculations to give coupling factors and

shape functions for other fuel enrichments. A Detailed description of these experiments is given in an unpublished memo.[35] Only a summary of these results is presented here.

Table 4-2 gives the coupling factors used for the HRR experiments. This data is presented as a function of fuel enrichment and polyethylene thickness. The axial and radial energy-deposition profiles are shown in Figures 4-5 and 4-6. In addition, the profile data is presented in tabular form for the axial profile (Table 4-3) and in polynomial form for the radial profile (Table 4-4). The same axial-energy-deposition profile was used for all types of fuel, pin enrichments, and polyethylene thicknesses.

Table 4-2 ACRR coupling factors for the HRR experiments*

| Experiment | Enrichment % | Neutron Modifier | Coupling Factor | |
|------------|-----------------|---------------------|-----------------|-----------------------|
| | | | J/g/MJ | J/cm ³ /MJ |
| HRR-2 | 67.2 | none | 13.85 | 138.70 |
| HRR-3 | 67.2 | none | 13.85 | 138.70 |
| HRR-5 | 40.5 | 3.18 mm poly | 13.38 | 133.10 |
| HRR-6 | 70.3 | none | 14.15 | 141.64 |

* Based on the 1980 reactor power calibration.

Because of limited experimental data, only estimates of the energy-deposition uncertainties are available. Two major sources of uncertainties exist. The first is the uncertainty associated with determining the measured fission density by the fission-product counting process. This uncertainty is estimated to be $\pm 7\%$. The other uncertainty is in the generalization of this measured result to other geometries and enrichments. This uncertainty is expected to be in the range of 1 to 3%. Thus, the overall uncertainty associated with the coupling factor is ± 7 to 8%.

In the spring of 1981, the ACRR power normalization was modified. This modification compensated for changes in the fuel loading. It also equated the average energy in the pulse mode (as measured by the core-temperature change) to the steady-state energy deposition (as measured by the change in pool-water temperature). Thus, future publications may list different coupling factors due to these changes.

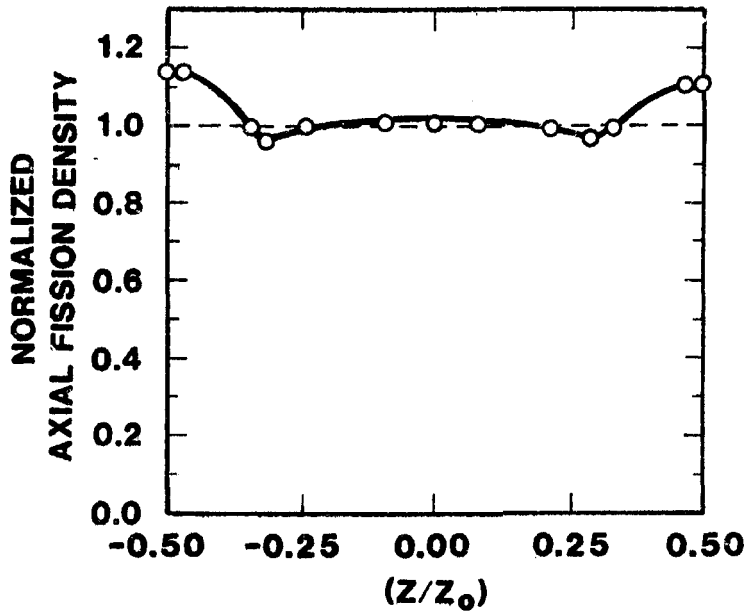


Figure 4-5 Axial-energy-deposition profile calculated by TWOTRAN-II: HRR series.

Table 4-3 Axial-energy-deposition profile for all HRR experiments

| z/z_0^* | 0.00 | 0.07 | 0.22 | 0.31 | 0.34 | 0.46 | 0.50 |
|--------------------------------------|-------|-------|-------|-------|-------|-------|-------|
| Norm. Energy Deposition [†] | 1.021 | 1.021 | 0.987 | 0.963 | 0.981 | 1.141 | 1.141 |

* Symmetric about center of sample ($z/z_0 = 0$)
 where z = distance from center of sample
 z_0 = 1/2 sample length

[†] Normalized such that $\frac{1}{2z_0} \int_{-z_0}^{z_0} E(z) dz = 1$

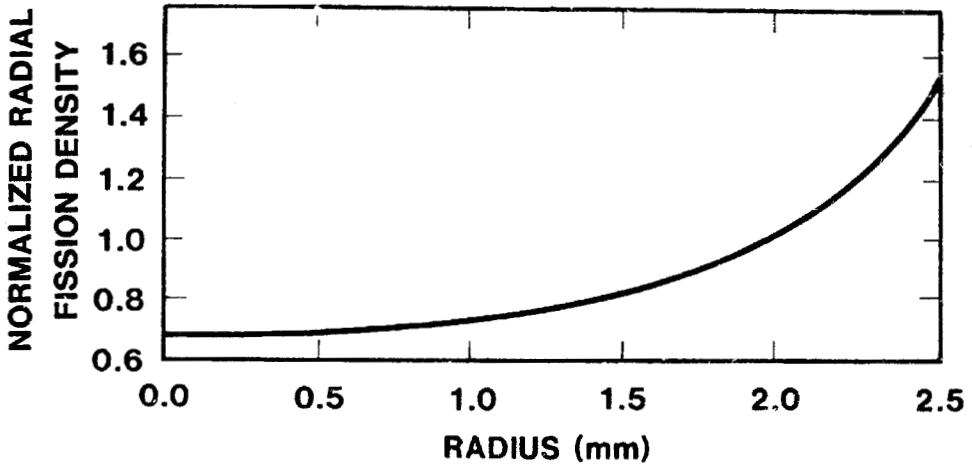


Figure 4-6 Typical radial-energy-deposition profile calculated by TWOTRAN-II (HRR-5 shown).

Table 4-4 Radial-energy-deposition profiles for HRR experiments

$$E(r)^* = a_0 + a_1 r + a_2 r^2 + a_3 r^3; \text{ (r in meters)}$$

| Experiment | a_0 | a_1 | a_2 | a_3 |
|------------|---------|----------------------|-----------------------|----------------------|
| HRR-2/3 | 0.58605 | 3.8328×10^2 | -3.4519×10^5 | 1.3401×10^8 |
| HRR-5 | 0.6850 | 2.5630×10^2 | -2.6920×10^5 | 1.1490×10^8 |
| HRR-6 | 0.49891 | 5.5309×10^2 | -4.6528×10^5 | 1.6254×10^8 |

* Coefficients normalized such that $\frac{2}{(r_{\max})^2} \int_0^{r_{\max}} E(r) r dr = 1$

5. EXPERIMENT RESULTS AND PRELIMINARY ANALYSIS

The experimental results and preliminary analysis for each of the HRR experiments are presented in this chapter. The discussion begins with a brief summary of the HRR transients and a comparison of the actual histories with the objectives as defined in Section 3.1. A listing of the major events observed during the experiments is also included. Most of the discussion of results and analysis can be found in the section on thermal analysis, Section 5.2. This section also includes the majority of the posttest analysis done to date. Some preliminary posttest fission gas analyses have likewise been performed, and these are described in Section 5.3.

5.1 Summary of HRR Transients

The ACRR power histories used in the HRR experiments consisted of two pulses separated by about 2.5 s of near constant-power operation. The first pulse and the subsequent constant-power operation were designed to melt off the cladding and result in a fuel-temperature distribution prototypic of the LOF accidents being investigated. During the tail end of the constant-power period, radiative heat losses from the fuel surface to the inner canister wall were very nearly balanced by the energy input. Thus, a quasi-equilibrium fuel-temperature distribution was achieved with an average temperature of 2100 to 2500 K in the outer, gas-bearing fuel region. During the second pulse, fuel heating rates on the order of 100 K/ms were achieved, and fuel disruption occurred.

The actual ACRR power histories used in experiments HRR-6, HRR-2, HRR-3, and HRR-5 are shown in Figures 5-1 through 5-4.

The high-speed camera, operating at 4000 to 10 000 frames per second, recorded the fuel behavior beginning approximately 1 s after the first pulse. Several major events were observed in the films for each experiment. The timing of these events is indicated in Figures 5-1 through 5-4. These events consist of: start of cladding melting (SCM), cladding meltoff (CMO), fuel swelling (FS), start of fuel disruption (SFD), and loss of pin geometry (LPG). These events are defined as follows:

- SCM: Start of cladding melting is the time at which clad draining is first observed.
- CMO: Clad meltoff is the time when ~ 90% of the fuel surface has been uncovered by draining of the molten clad.
- FS: The time of fuel swelling is the time at which gross fuel expansion (in excess of that which can be explained by thermal expansion) starts.

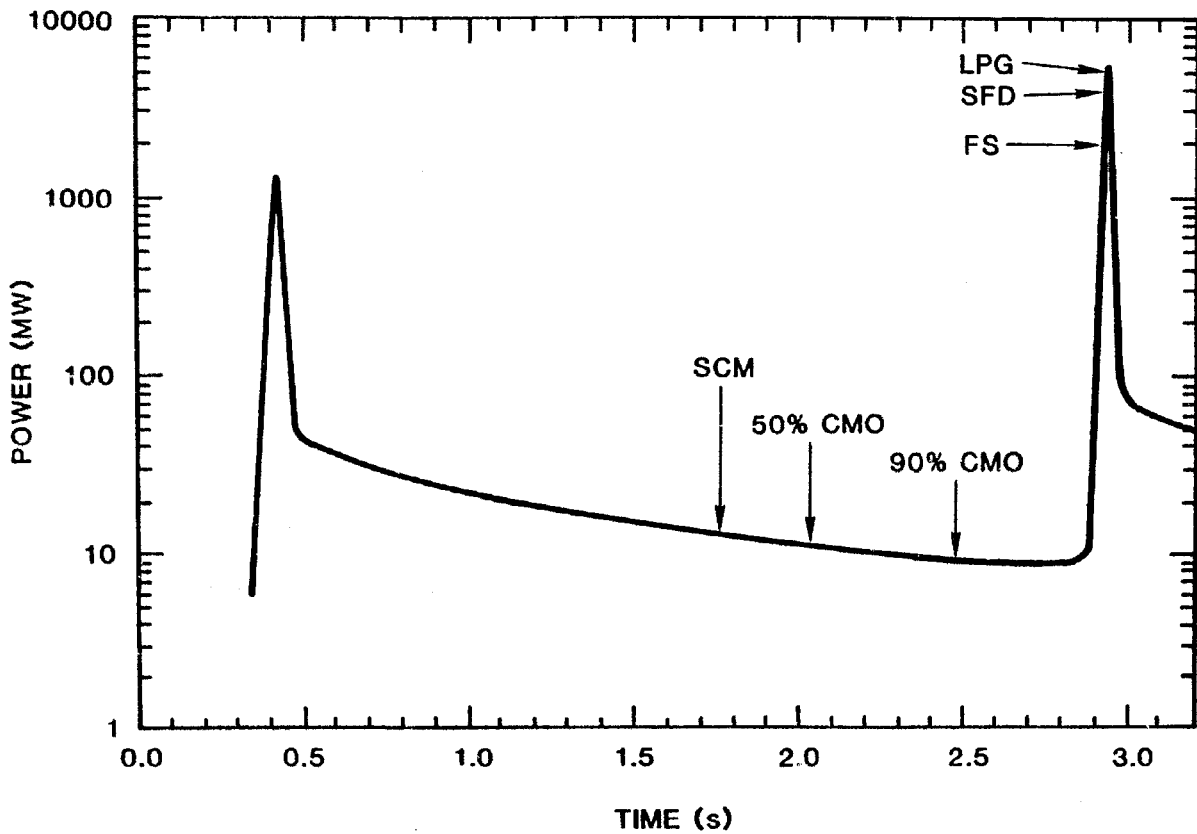


Figure 5-1 ACRR power history for HRR-6.

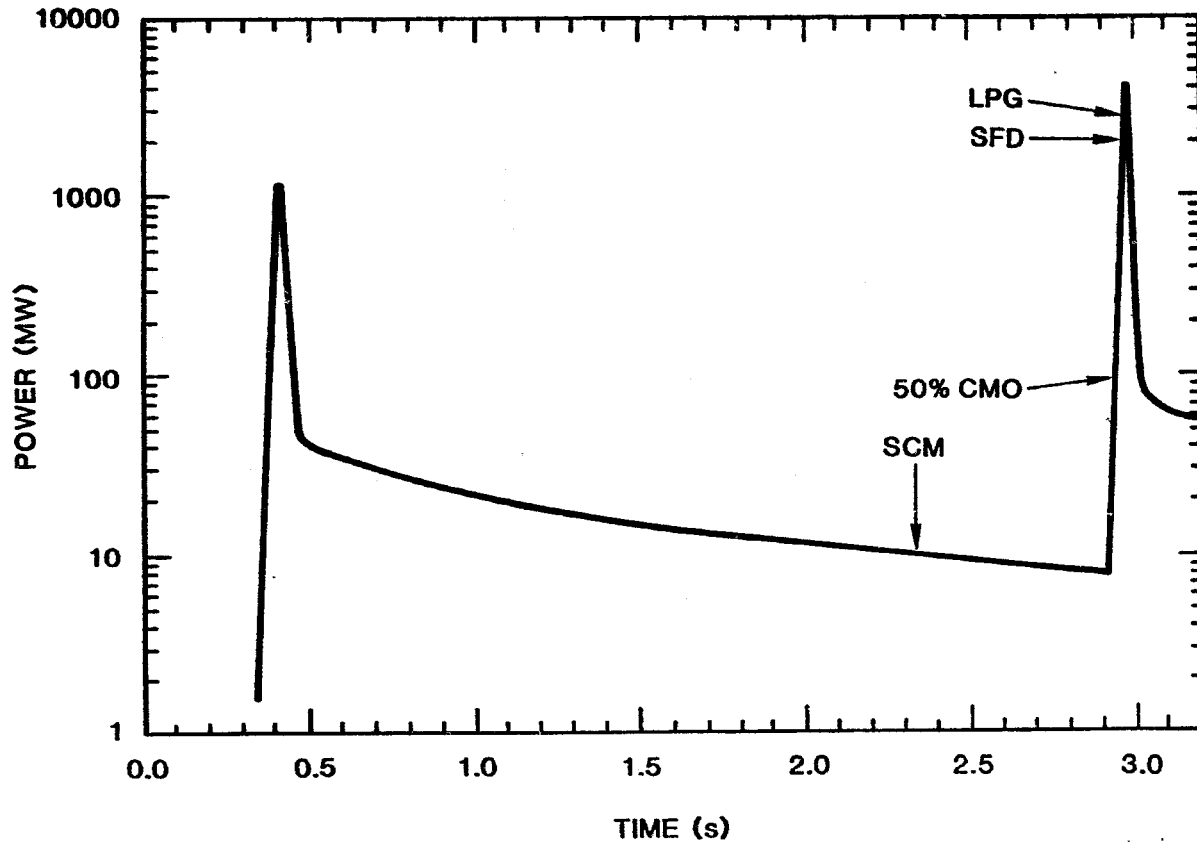


Figure 5-2 ACRR power history for HRR-2.

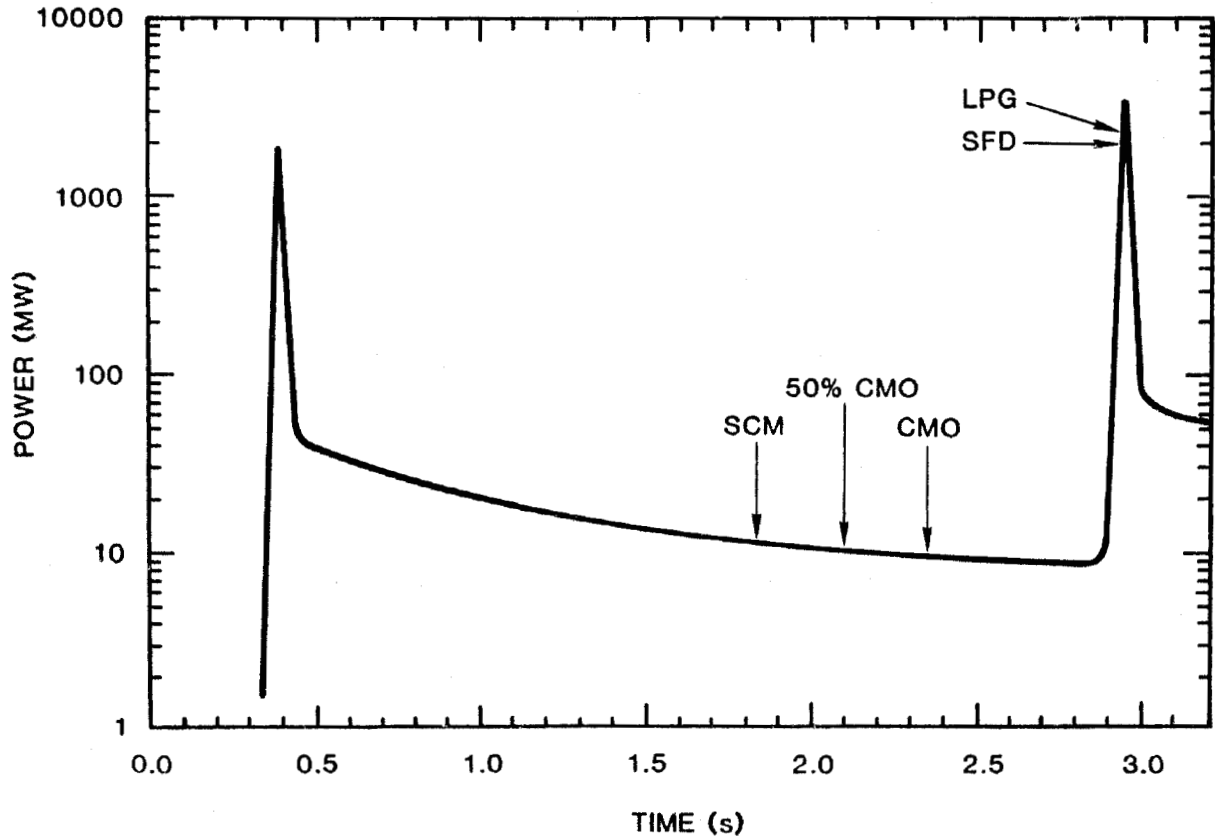


Figure 5-3 ACRR power history for HRR-3.

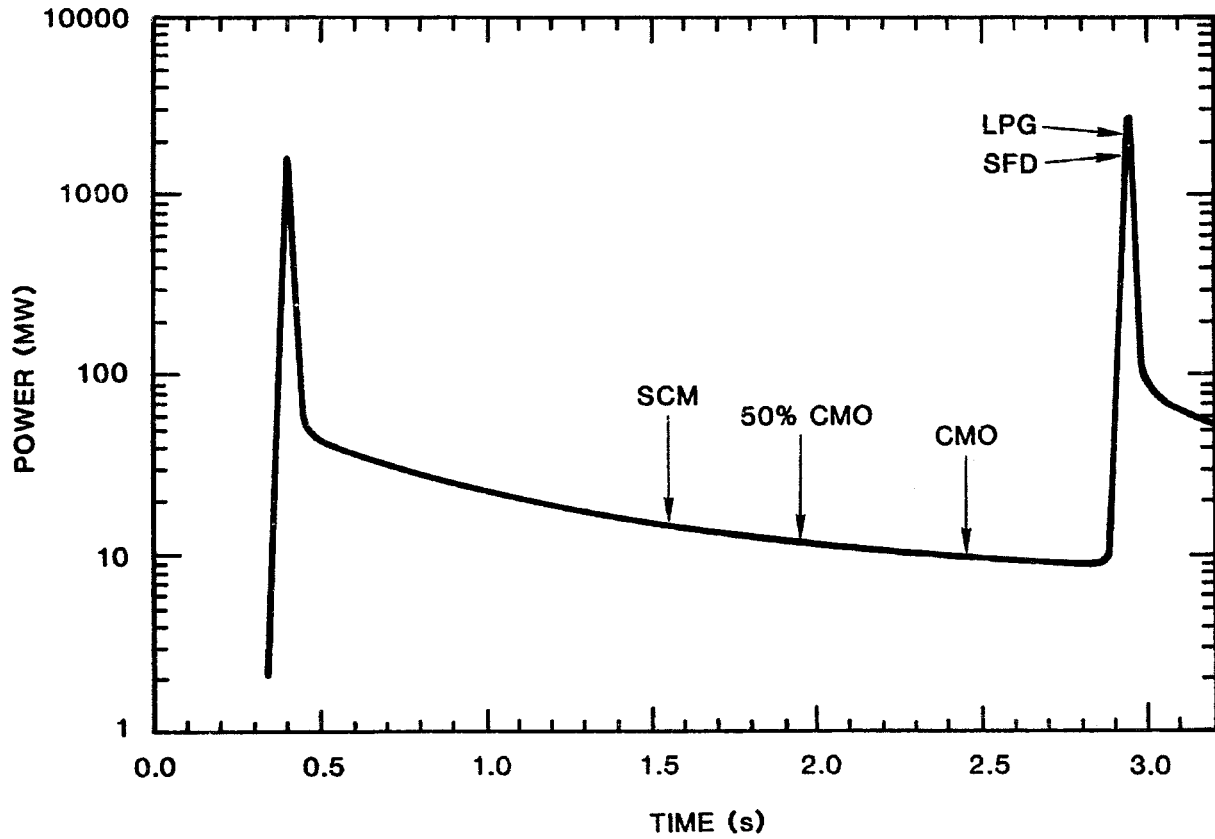


Figure 5-4 ACRR power history for HRR-5.

SFD: The start of fuel disruption is the time when the pellet stack rapidly begins to lose its cylindrical geometry.

LPG: Loss of pin geometry is the time when the fuel is no longer recognizable as a fuel pin, i.e., it begins to have spherical geometry.

A summary of the observed timing for these events is presented in Table 5-1. The timing of the events was determined from the films, and the selection of a specific frame to identify each event was somewhat subjective. Consequently, the times given in Table 5-1 have an associated uncertainty of ± 200 ms for CMO, ± 2 ms for FS, and ± 1 ms for SFD and LPG.

Table 5-1 Summary of event timing in HRR experiments

| Experiment: | HRR-6 | HRR-2 | HRR-3 | HRR-5 |
|-------------|----------|-------|--------|-------|
| Event | Time (s) | | | |
| SCM | 1.76 | 2.34 | 1.828 | 1.551 |
| 50% CMO* | 2.062 | 2.95 | 2.128 | 1.951 |
| CMO | 2.479 | † | 2.341 | 2.430 |
| FS | 2.9225 | # | # | # |
| SFD | 2.9255 | 2.959 | 2.9294 | 2.930 |
| LPG | 2.9285 | 2.962 | 2.9304 | 2.933 |

* Clad draining had exposed 50% of the fuel surface.

† Fuel disruption occurred prior to complete clad meltoff.

No significant fuel swelling was observed prior to disruption.

Because of enrichment differences between experiments, and because of the use of a polyethylene moderator in experiment HRR-5 (see Section 4.3), the coupling factors vary slightly between experiments. These coupling factors are again summarized in Table 5-2. Table 5-2 also lists the pin power at the peak of the first pulse, at the start of the second pulse (end of preheat), and at the peak of the second pulse, as well as the time between first and second pulse.

Table 5-2 Pin powers and reactor-pulse summary

| Experiment: | HRR-6 | HRR-2 | HRR-3 | HRR-5 |
|---|-------|-------|-------|-------|
| Parameter | | | | |
| Coupling Factor (J/g/MJ) | 14.15 | 13.85 | 13.85 | 13.38 |
| Pin Power* at Peak of Pulse 1 | 19.21 | 16.07 | 25.10 | 22.75 |
| FWHM [†] of Pulse 1 (ms) | 28.5 | 30.3 | 24.3 | 25.8 |
| Pin Power* at End of Plateau | 0.113 | 0.113 | 0.113 | 0.113 |
| Pin Power* at Peak of Pulse 2 | 71.25 | 59.03 | 48.17 | 38.86 |
| FWHM [†] of Pulse 2 (ms) | 17.8 | 20.0 | 21.8 | 23.9 |
| Time Between Pulse 1 and Pulse 2 (s) | 2.516 | 2.562 | 2.552 | 2.543 |

* Pin powers are in kW/g.

† FWHM = Full Width at Half Maximum.

Qualitatively, the appearance of disruption was very similar in each of the four experiments: a violent spray-like dispersal occurring well into the second power pulse. Thermal analysis, however, indicates that the timing of disruption relative to the time of fuel melting was different for the fresh- versus the irradiated-fuel experiments. These differences will be discussed in the next section.

Before getting into the details of the thermal analysis, it is worth comparing the actual HRR power/temperature histories to the objective as defined in Table 3-1. The parameters of interest are the gas-bearing-fuel temperature (taken as the temperature at a relative fuel radius of 0.8) at the end of the preheat, the length of the preheat, and the final temperature-ramp rate (taken at a fuel radius of 0.8 at SFD). These parameters are summarized in Table 5-3. As can be seen from these results, the test objectives were generally achieved although it was not possible to ensure the same temperature ramp rate during the second pulse for each experiment.

Table 5-3 HRR experiment matrix: Key parameters

| Experiment | Preheat Temperature* (K) | Preheat Time (s) | Temperature Ramp*† (K/ms) |
|------------|--------------------------|------------------|---------------------------|
| HRR-6 | 2320 | 2.5 | 90 |
| HRR-2 | 2296 | 2.5 | 60 |
| HRR-3 | 2478 | 2.5 | 50 |
| HRR-5 | 2480 | 2.5 | 45 |

* At a relative fuel radius of 0.8.

† Instantaneous ramp at the time of disruption.

5.2 Thermal Analyses

Detailed two-dimensional (radial-axial) thermal analyses were performed for each of the HRR experiments, using the TAC-2D code.[36] The cylindrical geometry modeled in these calculations is shown in Figures 5-5 and 5-6. Included are the fuel-pin segment with its associated cladding, the depleted UO₂ holders on each end of the pin, the helium fill gas, and the aluminum canister. Inspection of the TAC-2D results indicated that axial conduction had little effect on the calculated temperature distribution near the axial midplane of the test pin segment. Since that region of the pin was the hottest and first to disrupt, it was possible simply to perform one-dimensional (radial) heat-conduction calculations for the centermost fuel pellet only. These one-dimensional calculations were performed using the thermal module from the SANDPIN code.[5] Because of a more accurate treatment of fuel melting, cladding melting, and thermal radiation, these SANDPIN calculations form the basis for the discussion that follows.

The SANDPIN calculations were performed using the power histories shown in Figures 5-1 through 5-4. The coupling factors and energy-deposition profiles that were used were discussed in Section 4.3. The calculations used standard temperature-dependent material properties[37] and a gap model[38] that accounted for temperature-dependent gap-gas conductivity, gap opening/closure caused by relative fuel-cladding thermal expansion, and radiation heat transfer. The fuel microstructure used in the calculations is as summarized in Section 3.2.

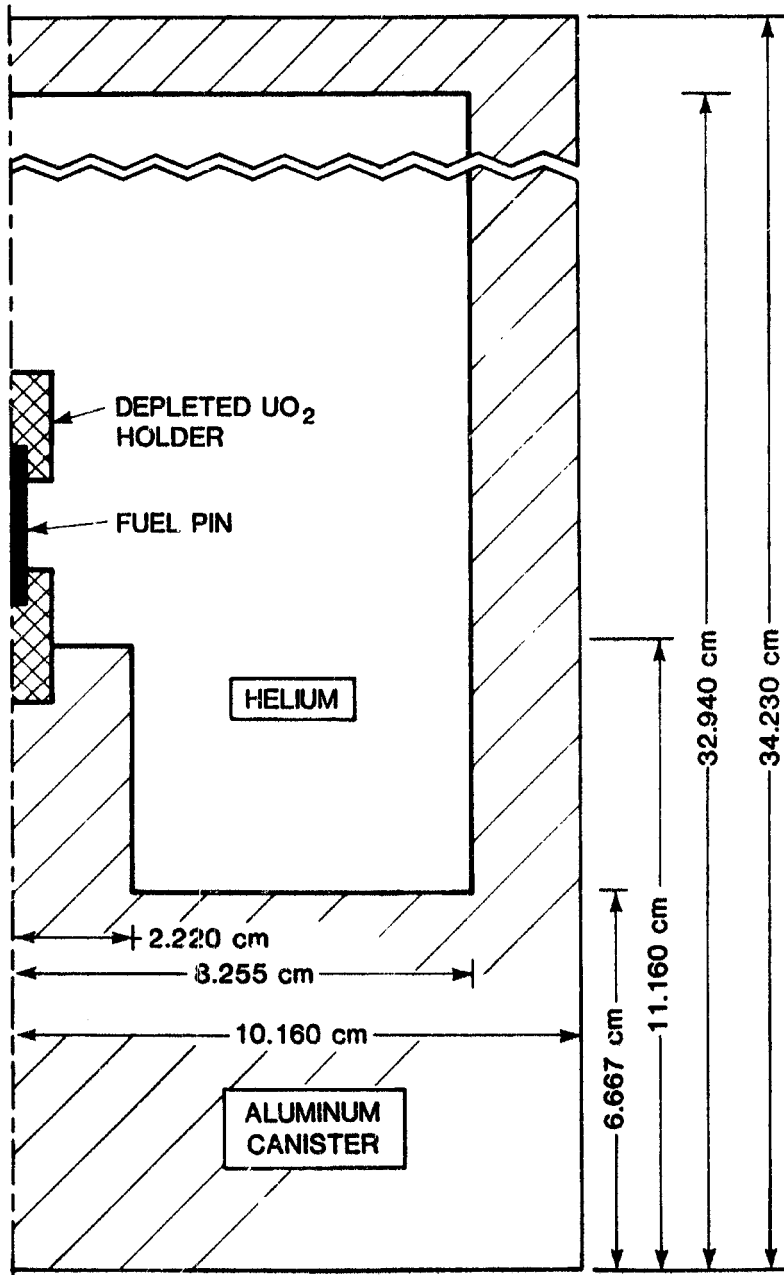


Figure 5-5 Geometry modeled in thermal analyses.

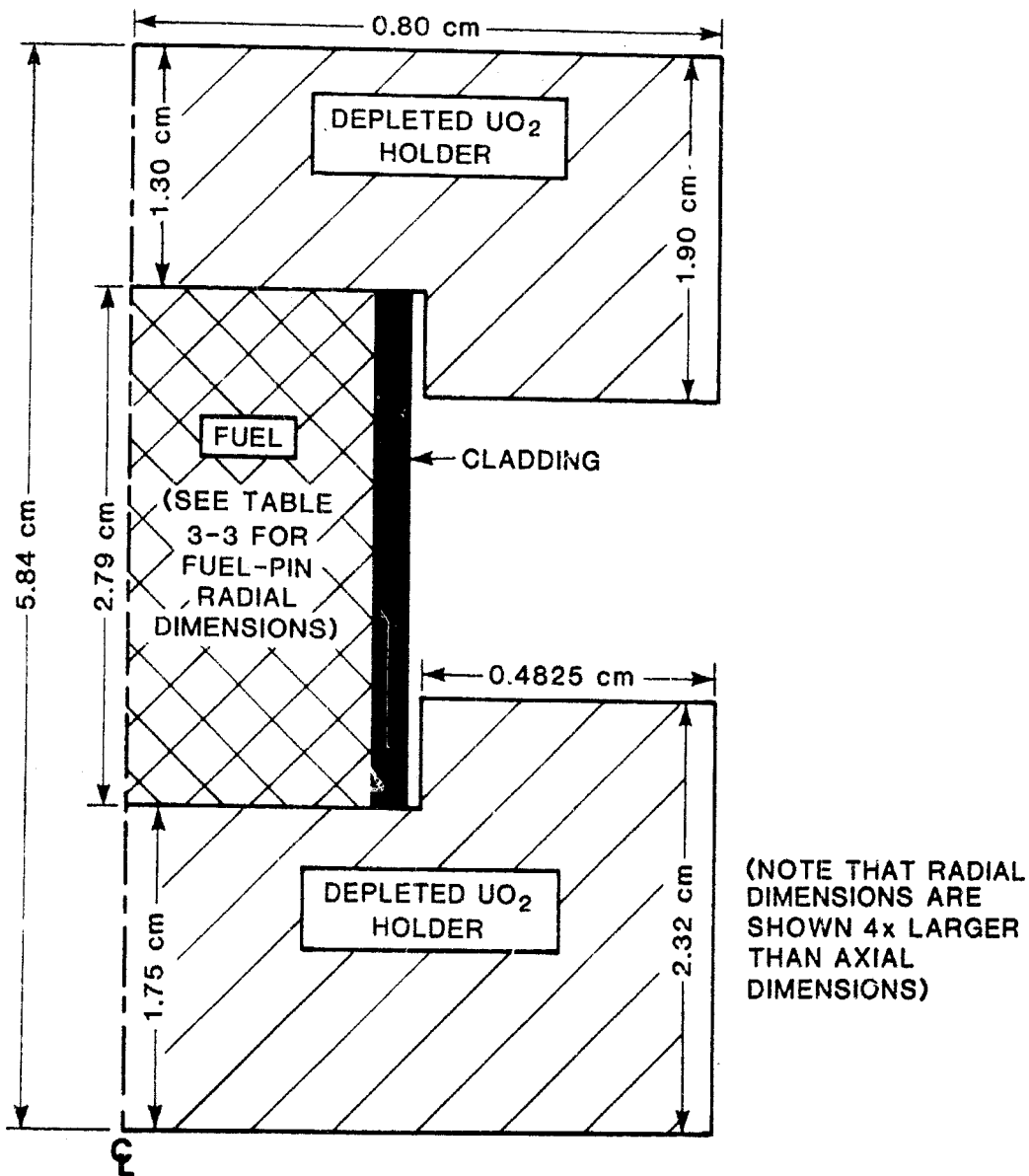


Figure 5-6 Geometry for fuel pin and holder.

In each of the transients, the gas both in the fuel-cladding gap and between the cladding and canister was initially helium at 0.03 MPa pressure. This was the gas composition used for each transient throughout the calculations. In reality, however, transient fission-gas release occurring in the irradiated experiments (HRR-2, -3, -5) contaminated the helium gas and lowered the effective gas conductivity. This time-dependent gas composition change is not currently modeled in the SANDPIN code.

Before describing the detailed results of the heat-transport calculations, it is important to summarize the major uncertainties in these calculations and their interpretation. Three sources of uncertainty have been identified. They result from the determination of the coupling factor, the alignment of the timing between films and power histories, and the selection of the film frame in which a major event is said to occur (e.g., the start of fuel disruption). Because the calculations indicate that fuel disruption in all the experiments occurred near the time of fuel melting, the three uncertainties identified will be put into perspective by considering their effect on the calculated melt fraction.

The uncertainty in the coupling factor is estimated to be no more than $\pm 8\%$. This uncertainty is absolute in the sense that it does not change from experiment to experiment. Consequently, it need not be given much consideration when comparing events or timings between different experiments. However, when trying to estimate quantities such as average fuel enthalpy or melt fraction, it should be considered. At the time of fuel melting, the total energy deposition in the fuel is approximately 1000 J/g. An 8% uncertainty in this value is 80 J/g, or about 30% of the heat of fusion.

The second source of uncertainty occurs because of a mismatch in the alignment of the timing in the films with the timing of the measured reactor power. For all experiments, this uncertainty is estimated to be ± 1 ms. Near the start of fuel disruption, the energy deposition rate is approximately 2.8×10^4 W/g. Therefore, a 1-millisecond error in the timing alignment results in a 28 J/g uncertainty in the energy deposition. This corresponds to approximately 10% of the heat of fusion.

The third source of uncertainty is in the selection of the frame that corresponds to the initiation of an event. For example, selection of the frame corresponding to the start of fuel disruption or to the initiation of fuel swelling entails some judgment concerning when these events begin. For the analysis here, it is estimated that this uncertainty is approximately ± 1 ms.

Thus, relative comparisons between experiments (e.g., melt fraction at the start of fuel disruption between fresh and irradiated fuel) require consideration of only the last two uncertainties. In this situation, the uncertainties combine to give a total uncertainty of $\pm 14\%$ of the heat of fusion. However, when characteristics are considered in an absolute sense (e.g., the absolute uncertainty at SFD), all three types of uncertainties must be considered. In this case, the total uncertainty is 33% of the heat of fusion.

5.2.1 Analysis of Fresh-Fuel Experiment HRR-6

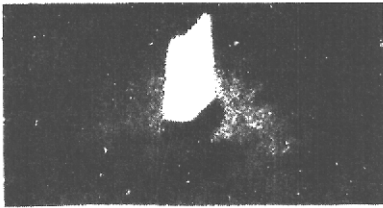
The reactor power transient used in the HRR-6 experiment is shown in Figure 5-1. The high-speed camera recorded the events occurring during the transient at a filming rate of 4000 frames per second. Photos (from this film) of the major events discussed in Section 5.1 are shown in Figure 5-7. These events are CMO ($t = 2.479$ s, Figure 5-7a), FS ($t = 2.9225$ s, Figures 5-7b and 5-7c), SFD ($t = 2.9255$ s, Figure 5-7d), and LPG ($t = 2.9285$ s, Figure 5-7e). As previously noted, there is a judgmental uncertainty of ± 200 ms associated with CMO, ± 2 ms with FS, and ± 1 ms with SFD and LPG.

The SANDPIN thermal module was used to calculate the time-dependent temperature distributions in the fuel-pin segment. Figure 5-8 shows the calculated and measured fuel-surface temperature as a function of time. The optical pyrometer was used to determine the measured fuel-surface temperature. Unfortunately, this device was not accurately calibrated; consequently, an adjustment of the data had to be made. For both the calculated and measured surface-temperature histories, the curves exhibit a plateau around 2.925 to 2.927 s. The calculations clearly indicate this plateau resulted from fuel melting near the fuel surface. Therefore, it was concluded that the observed plateau occurred near the melt temperature, and the temperature measured by the pyrometer at 2.926 s was set at 3021 K (halfway between solidus and liquidus). The choice of 3021 K (rather than the solidus temperature of 2998 K or the liquidus temperature of 3043 K) was completely arbitrary. In fact, the calculations indicate that the surface-temperature plateau was closer to ~ 3000 K.

The temperature as "seen" by the pyrometer is not really the surface temperature but rather some average of the temperature in a thin outer crust. This is because the pyrometer actually sees into the fuel a short distance. This effect is caused by the presence of numerous fuel-surface cracks and the partial transparency of UO_2 at high temperatures.[39] To illustrate the possible effect such penetration could have on the results, the calculated temperature is plotted not only for the fuel surface but also for a point 0.035 mm into the fuel (see Figure 5-8). For reference, the pin power is also shown.

In general, the agreement between measured and calculated fuel-surface temperature is excellent. For most of the transient from 2.900 s to 2.927 s, the discrepancy between the plotted pyrometer data and the calculated temperature band is on the order of 20 to 40 K. This could simply be a result of the arbitrary choice of 3021 K at 2.926 s for the pyrometer data, or a result of the $\pm 8\%$ uncertainty in coupling factor.* The important thing to notice is that the calculation and the measured data agree to within < 1 ms on the start of the melting plateau near 2.925 s.

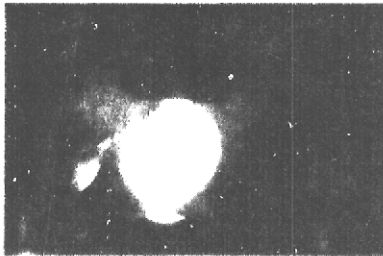
*The timing uncertainty of ± 1 ms, and the qualitative uncertainty of > 1 ms associated with defining event times, do not affect these comparisons because they are strictly associated with the film timing. The timing uncertainty between the power history (calculated results) and the pyrometer data is essentially zero.



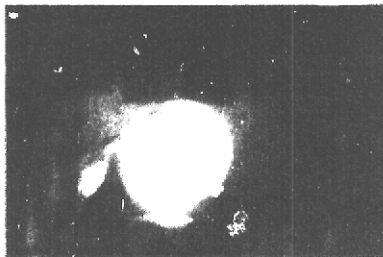
a. Clad meltoff (CMO),
 $t = 2.479$ s.



b. Fuel swelling (FS),
 $t = 2.923$ s.



c. Fuel swelling (FS),
 $t = 2.925$ s.



d. Start of fuel disruption (SFD),
 $t = 2.926$ s.



e. Loss of pin geometry (LPG),
 $t = 2.929$ s.

Figure 5-7 Photos of major events for experiment HRR-6.

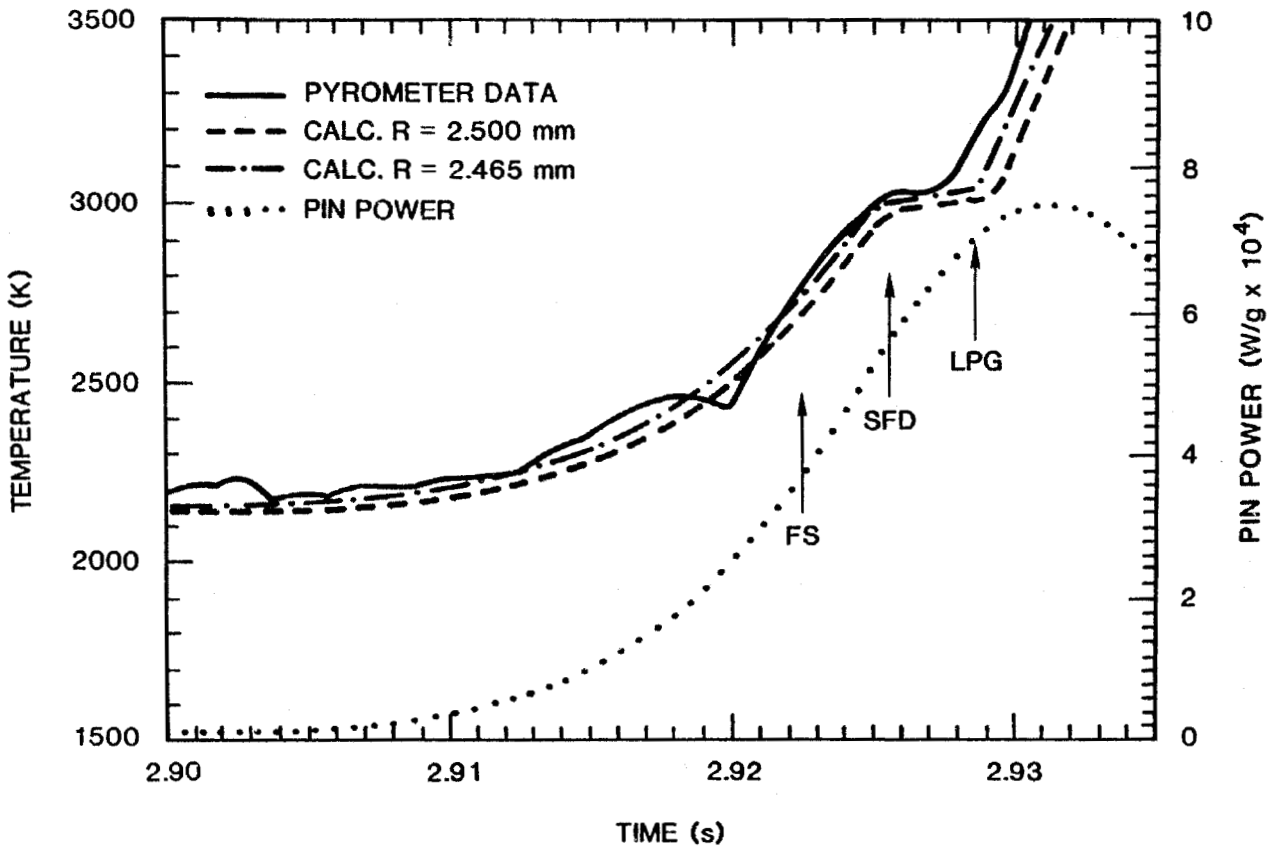


Figure 5-8 HRR-6 fuel-surface-temperature history.

Two areas of disagreement between the pyrometer data and the measured temperatures are apparent in Figure 5-8. The first of these occurs around 2.920 s, when the pyrometer data seems to exhibit an oscillation. While the exact cause of this perturbation has not been determined, it is suspected that it resulted from vibration in the optical system. The second area of large disagreement (> 50 K) between measured and calculated temperature can be seen starting at 2.928 s. However, the comparison is no longer meaningful here because the calculation still assumes cylindrical geometry, whereas in reality the fuel has dispersed into a near-spherical "cloud". Because of this fuel dispersal, the effective reactor coupling factor increases, and more energy is being deposited in the fuel than is accounted for in the calculation. Thus, one would expect the calculated temperature to lag behind the measured pyrometer data. In addition, it is not clear at this point exactly what fuel the pyrometer is seeing, because of the low density of the expanding fuel cloud and the nonuniformity of the expansion.

Aside from the arbitrary calibration of the pyrometer data, the 20 to 40 K discrepancy between measured and calculated data may partially be a result of the $\pm 8\%$ uncertainty in power-coupling coefficient. The effect of this uncertainty can be seen in Figure 5-9. Plotted are the pyrometer data along with the surface temperature calculated using the nominal coupling factor, a value that was 8% high, and a value that was 8% low. The temperature plateau around 2.926 s occurs at the same temperature for each value of the coupling factor used. The primary effect of the 8% variation in coupling factor is to change the fuel temperature at the end of the preheat (2.900 s) by approximately ± 80 K and to shift the timing of the melt plateau at 2.926 s by about ± 1 ms. Inspection of the curves in Figure 5-9 shows that the best qualitative agreement between pyrometer data and calculated temperature is obtained using the nominal value of the coupling factor. Based on these comparisons, it is concluded that the actual coupling factor applicable to the HRR-6 transient is in fact very close (within 2 to 3%) to the nominal value of 14.15 J/g/MJ assumed in the calculations.

The surface-temperature data discussed above are of little direct use in the interpretation of the experiment results. The radial-temperature distributions are needed for such interpretation. However, the excellent agreement between measured and calculated surface temperatures does provide some assurance of the validity of the temperature profiles calculated. Without this comparison there is no check on the accuracy of the thermal calculations.

The major events observed during the transients were shown in Figure 5-7. The calculated radial-temperature profiles corresponding to the times of these events are plotted in Figure 5-10. The radial distribution at the end of the preheat (EOP) is also shown.* These calculated temperature profiles are an important part of the overall

* Note that after clad meltoff, the clad temperatures were still plotted, but they are equal to the fuel-surface temperatures.

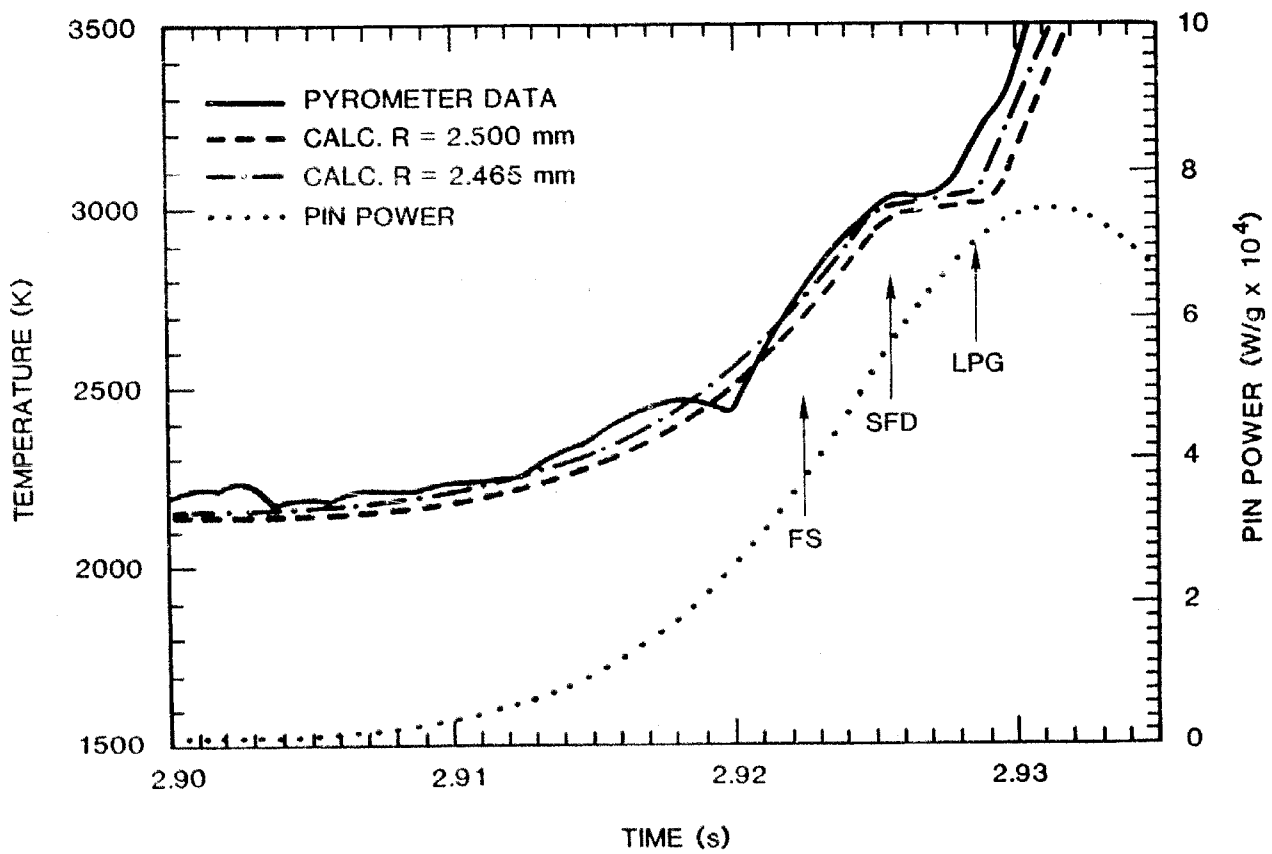


Figure 5-9 Effect of coupling-factor uncertainty on HRR-6 fuel-surface temperature.

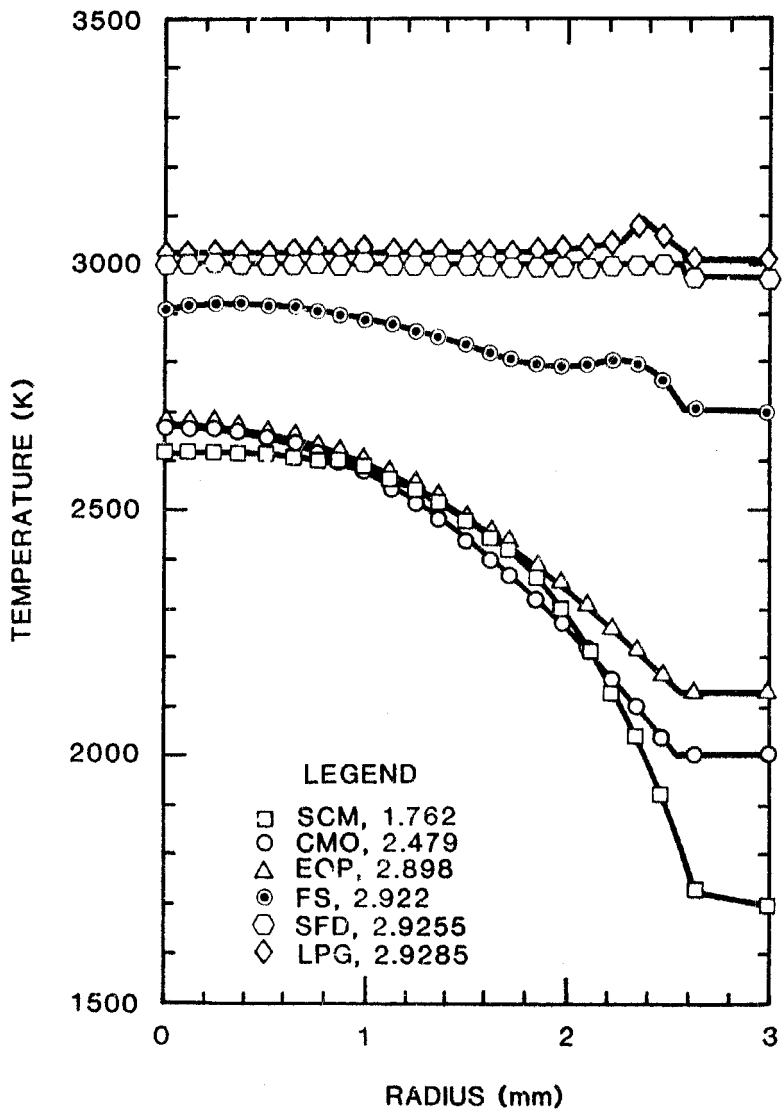


Figure 5-10 HRR-6 radial-temperature profiles.

interpretation of the observed behavior. In addition to the major events, several minor events were also observed. These are vertical fuel cracking, gaseous release, and some small-scale sputtering. A brief discussion of all events is given below.

The first major event observed in the film is fuel swelling. Figure 5-8 shows that the measured start of fuel swelling coincides with the outer portion of the fuel reaching ~ 2700 K. This swelling may be due to rapid high-temperature creep, which becomes important at fuel temperatures above ~ 2700 K.[40] The observed fuel swelling near the time of fuel disruption is shown in Figure 5-11. Prior to 2.9225 s, the increase in fuel-pellet diameter is minimal and can be explained by simple thermal expansion. Averaging the total 15 to 20% diametral expansion over the ~ 3 ms swelling time gives an average diametral "strain rate" of ~ 50 to 70 %/s. Investigators are working on determining the internal pressure source responsible for this observed swelling. Contaminant and fabrication gases (e.g., CO and He) are currently thought to be the most likely explanation.

At 2.9255 s, following ~ 3 ms of rapid fuel swelling, the start of fuel disruption is observed. A photo of the fuel at this time is shown in Figure 5-7d. As can be seen in Figure 5-8, both the pyrometer data and the thermal calculation indicate that the surface temperature at that time was going through a plateau caused by melting. The calculated radial-temperature profile at that time (Figure 5-10) shows that the melt front had reached $\sim 100\%$ of the fuel radius. The total melt fraction (fractional enthalpy through the heat of fusion, averaged over fuel mass) at this time is $\sim 11\%$. At the time of SFD, the linear expansion rate of the expanding fuel "cloud" is ~ 1.0 m/s, for an effective diametral "strain rate" of ~ 400 %/s.

The very qualitative "loss of pin geometry" occurs at ~ 2.9285 s. A photo of the fuel at this time is shown in Figure 5-7e, and the radial temperature profile is shown in Figure 5-10. The calculation is only qualitatively correct, because the severely disrupted geometry is not modeled in the calculation. However, at this time the outer part of the fuel has passed through the heat of fusion and is increasing in temperature at a rate of approximately 150 K/ms (see Figure 5-10). The peak fuel temperature of 3150 K has now essentially reached the 0.03 MPa boiling point of 3200 ± 200 K. Thus, it is suspected that the disruption mechanism has changed from phenomena associated with melting to one dominated by fuel boiling (vapor pressure). Further evidence for this is seen in the rapid change in the rate of fuel expansion that also occurs at this time. Figure 5-11 shows that the observed linear expansion rate of the expanding fuel "cloud" increased dramatically from ~ 1.25 m/s to ~ 20 m/s at the time of LPG. This rapid increase in the rate of fuel dispersal is consistent with a sudden increase in fuel-vapor generation as the fuel temperature reaches the 0.03 MPa boiling point.

In addition to these major events (fuel swelling, fuel disruption, and loss of pin geometry) several minor events were also observed, including radial fuel cracking, gaseous release, and fuel sputtering. In all likelihood, the secondary events played a less important role in the disruption process.

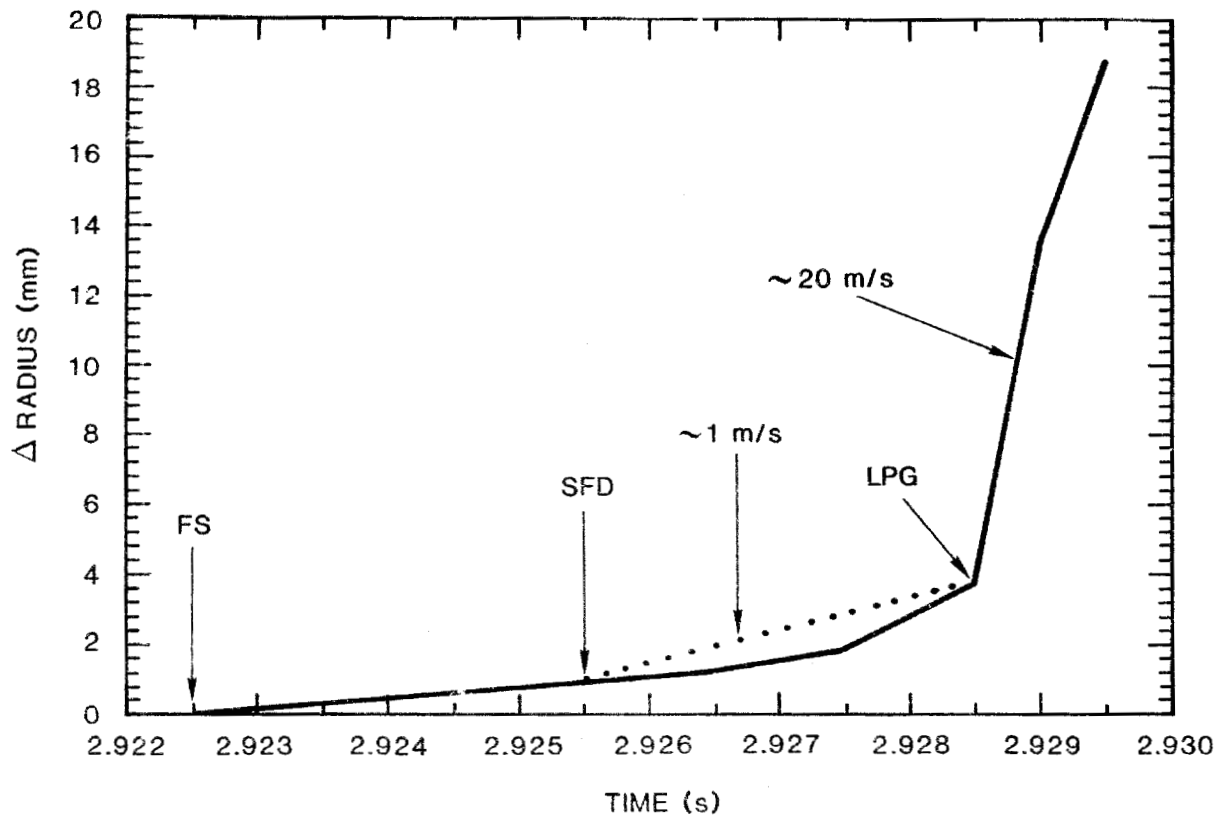


Figure 5-11 Fuel-expansion data for experiment HRR-6.

A vertical crack in the fuel surface was visible after clad melt-off occurred. At this time the fuel surface was still cool (i.e., ~ 2000 K), and the crack was visible because the interior of the fuel was much hotter than the surface. The crack appeared as a bright line on the surface and remained visible until 2.92 s, when the surface temperature reached ~ 2700 K. At this time the crack may have closed, or the radial fuel temperature gradient may have been too low to provide sufficient contrast between the hot inner fuel and the cool outer surface. The times of crack initial appearance and final disappearance correspond roughly to figures 5-7a and 5-7b, but unfortunately, the crack is not visible in the reproductions.

The gas release, which can be seen in Figure 5-7c, is unexplained at present. It may have been glowing noncondensable gases or possibly the fog or condensation of a gas emitted from the fuel just prior to SFD.

The sputtering of the fuel occurred near the time of SFD. The particle sputtered from the surface had a mass of approximately 5 mg and traveled with a constant velocity of 3.2 m/s. This small particle was very near the solidus temperature at the time of ejection and eventually reached the melt temperature 3 ms after ejection. The cause of the ejection has not yet been determined.

Among the events observed, the most important observation is that the fresh fuel used in the HRR-6 experiment disrupted near the time of 100% fuel melting,* significantly prior to fuel-vapor-pressure generation. This is seen very clearly in the radial temperature distribution at the time of initial fuel disruption (SFD) in Figure 5-10. The maximum fuel temperature at this time was 3012 K, which occurred when the fuel was only 33% through the heat of fusion. The fuel-vapor pressure at this point was only 0.004 MPa, well below the 0.03 MPa fill-gas pressure.

Further evidence for the absence of significant fuel-vapor pressure at the time of fuel disruption can be obtained from the pressure-transducer measurements of the inner canister pressure, shown in Figure 5-12. No evidence of any pressurization was seen until 2.932 s, about 6 ms after the start of fuel disruption. At that time, the peak calculated fuel temperature was 3700 K, about 500 K above the boiling point of the mixed-oxide fuel at 0.03 MPa. The rise in pressure seen at this later time was probably caused by fuel vaporization.

Thus, initial fuel disruption occurred about 3 ms before the calculations indicate that fuel boiling starts and about 6 ms before any significant fuel-vapor pressure was seen by the pressure transducer. However, at a higher ambient (capsule) pressure, this time difference between SFD and the onset of rapid fuel vaporization (boiling) could be significantly increased. In future experiments, higher ambient pressures will be used to separate effects (in time and temperature) caused by fuel melting and by fuel vaporization (boiling).

* Fractional area of the fuel above the solidus temperature of 2998 K.

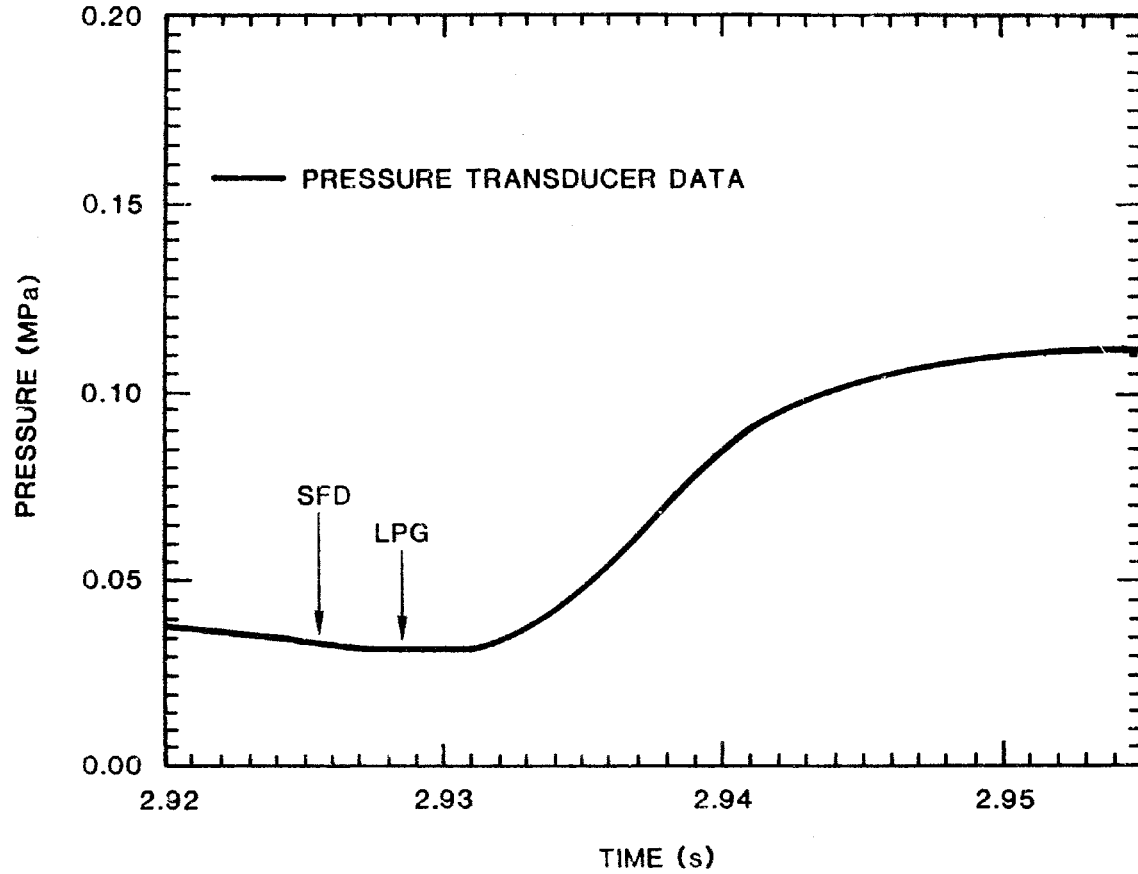


Figure 5-12 HRR-6 pressure-transducer history.

5.2.2 Analysis of Irradiated-Fuel Experiments HRR-2, -3, -5

As described in Section 3.1, the reactor power transients used for the irradiated-fuel experiments were very similar to the one used in the fresh-fuel experiment. The ACRR power histories used in experiments HRR-2, HRR-3, and HRR-5 are shown in Figures 5-2, 5-3, and 5-4. The observed fuel behavior was very similar for each of these three experiments, so a separate discussion of each experiment is not provided. Basically, the observed sequence of events was very similar to that of HRR-6. The major differences are that significant fuel swelling prior to disruption was not observed and that the observed disruption occurred slightly earlier (at a lower fuel melt fraction) in the irradiated-fuel experiments. The timing of the observed major events (CMO, SFD, and LPG) is summarized in Table 5-2.

The SANDPIN thermal module was used to calculate the time-dependent temperature distributions for each of the experiments. Figures 5-13, 5-14, and 5-15 show the measured and calculated fuel surface temperatures for experiments HRR-2, HRR-3, and HRR-5, respectively. Also shown are the reactor power transients and time markers indicating SFD and LPG. As for the HRR-6 analysis, the measured temperature is shown both for the fuel surface as well as for a point 0.035 mm into the fuel. The optical pyrometer was not available in the irradiated-fuel HRR experiments, so the measured temperatures were obtained from optical-densitometer measurements of the film exposure. These plotted densitometer measurements were not calibrated to the calculation as was done for the optical pyrometer data in the HRR-6 analysis. Thus, these measurements are the actual data and have an associated uncertainty of ± 100 K.

In general, the agreement between the measured and calculated temperatures is very good. The difference between the two curves is typically well within the ± 100 K uncertainty of the densitometer data.

The calculated radial temperature profiles at EOP, at SFD, and at LPG, are shown in Figures 5-16, 5-17, and 5-18 for each of the irradiated-fuel experiments HRR-2, HRR-3 and HRR-5. As for the HRR-6 analysis, these calculated results form the basis for the interpretation of the experiments.

Only minimal fuel swelling prior to disruption was observed in the irradiated-fuel experiments (less than 5 volume percent). In the fresh-fuel HRR-6 transient, the start of fuel swelling coincided with the surface temperature reaching ~ 2700 K. In the irradiated-fuel experiments, however, the start of fuel disruption occurred when the surface temperature was ~ 2700 K.

Photos of the fuel-disruption process are shown in Figures 5-19, 5-20, and 5-21 for experiments HRR-2, HRR-3, and HRR-5, respectively. In all cases, the disruption appeared as a gas-driven expansion of very small (< 0.1 mm) particles moving at speeds near 5 m/s. Qualitatively, there was little if any difference between the appearance of the disruption in the fresh- and irradiated-fuel experiments. The

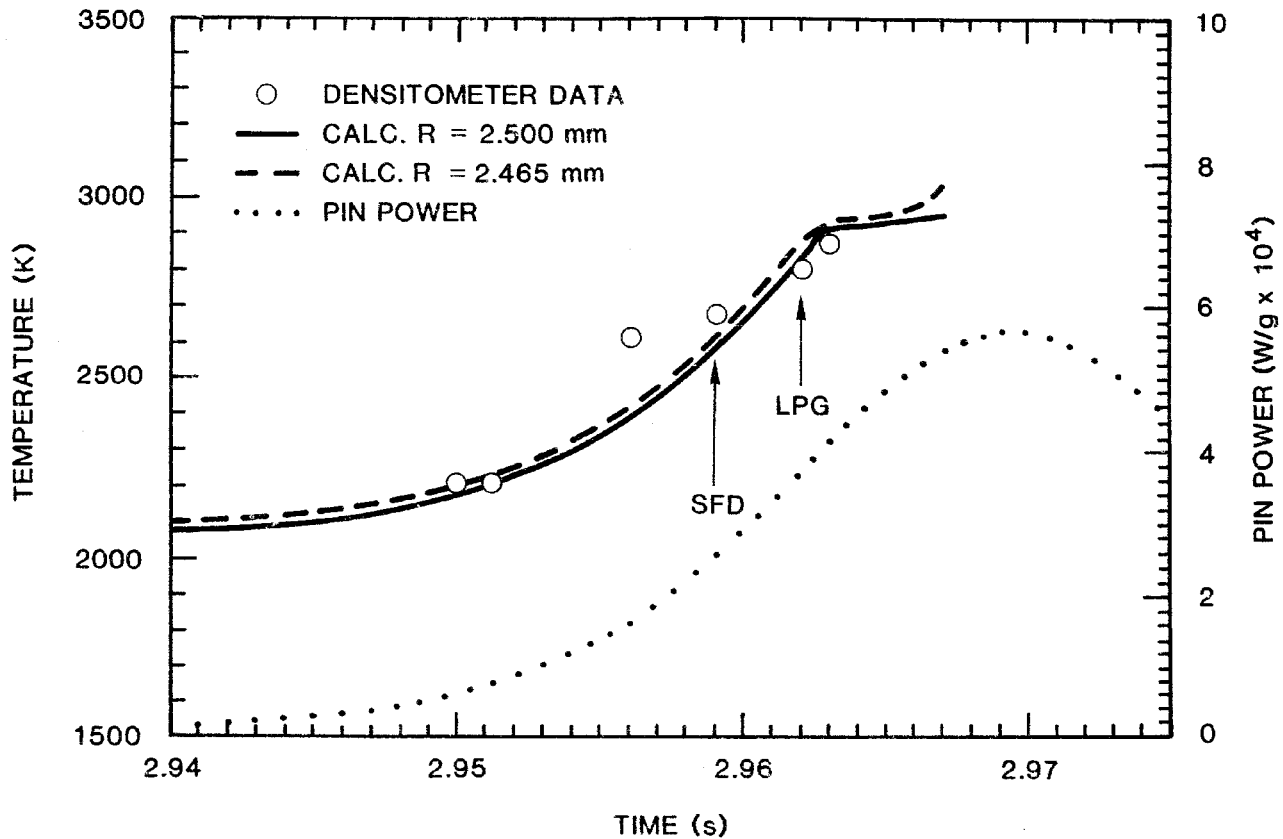


Figure 5-13 HRR-2 fuel-surface-temperature history.

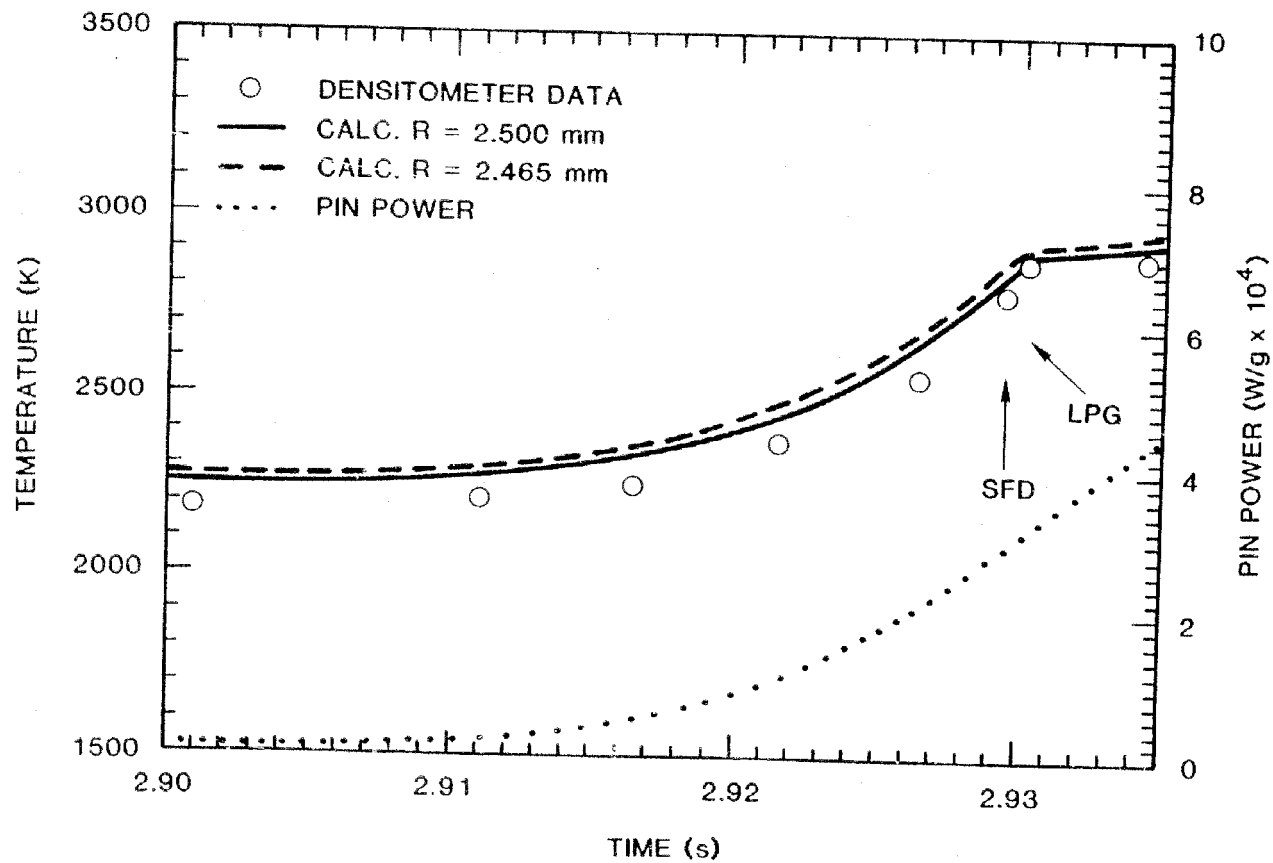


Figure 5-14 HRR-3 fuel-surface-temperature history.

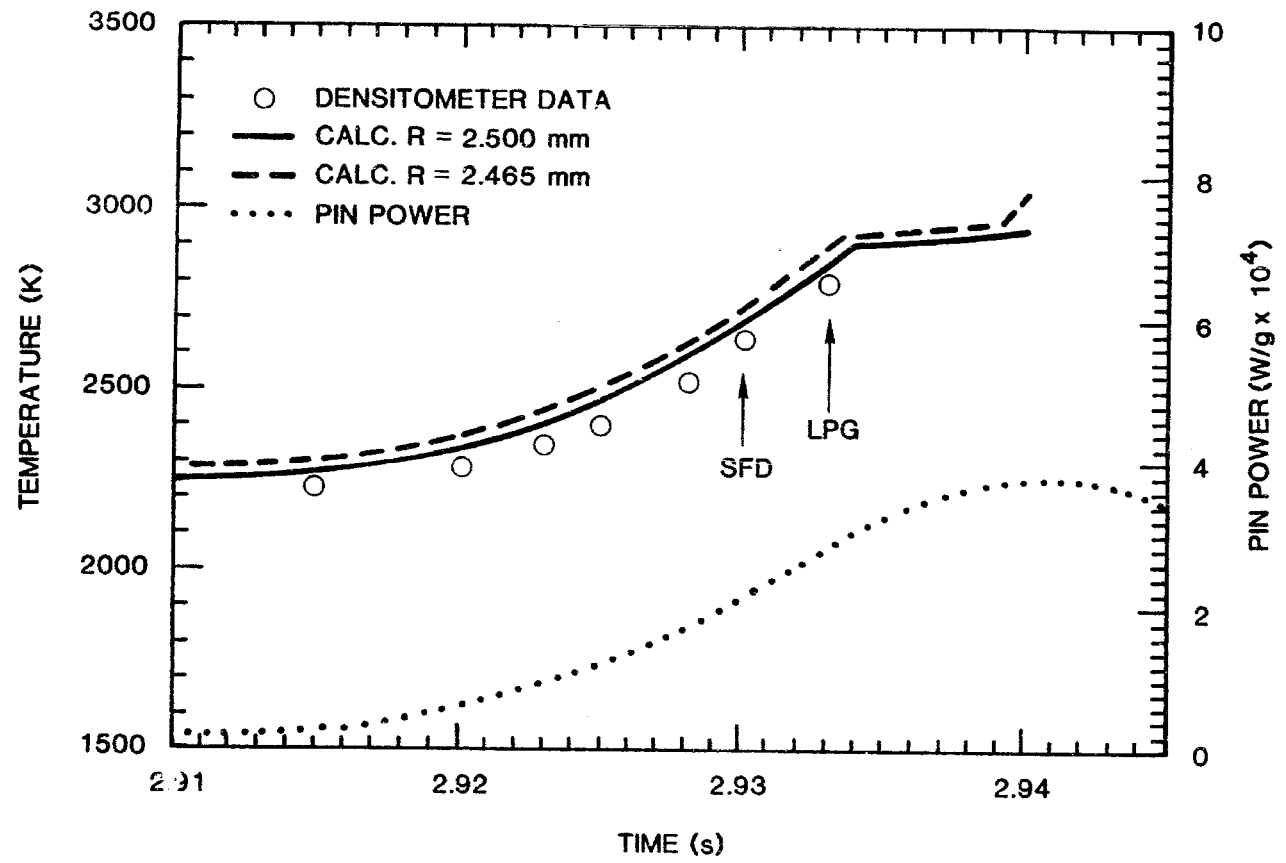


Figure 5-15 HRR-5 fuel-surface-temperature history.

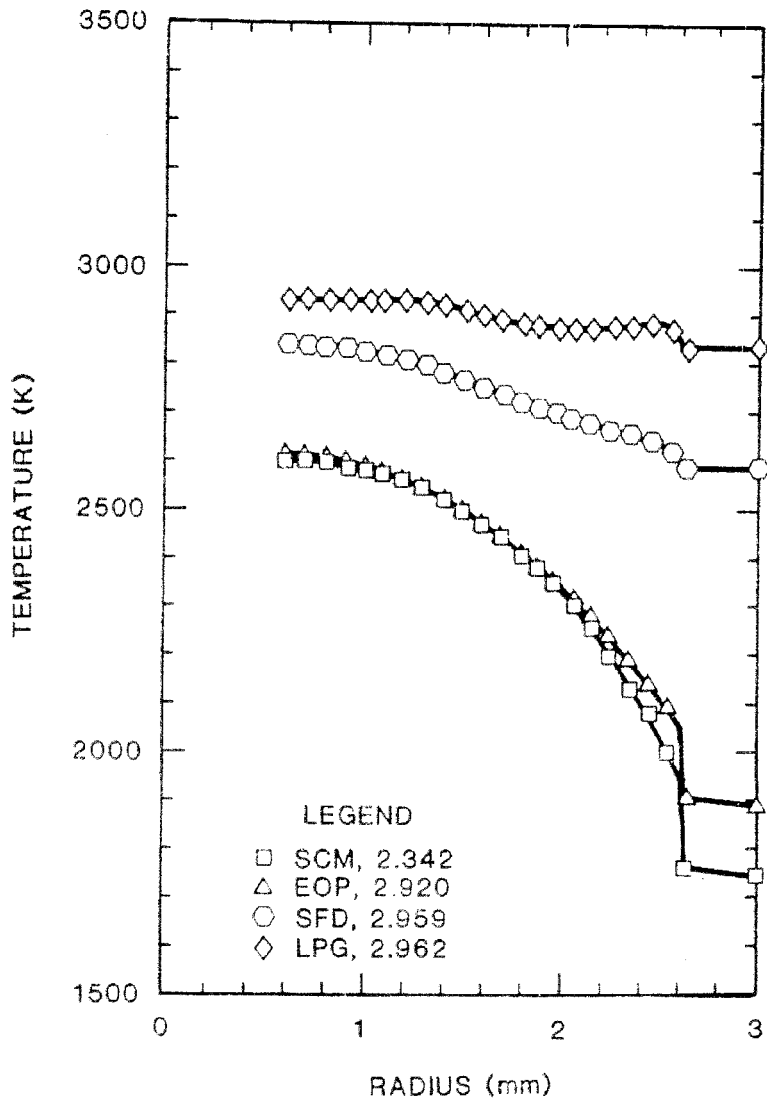


Figure 5-16 HRR-2 radial-temperature profiles.

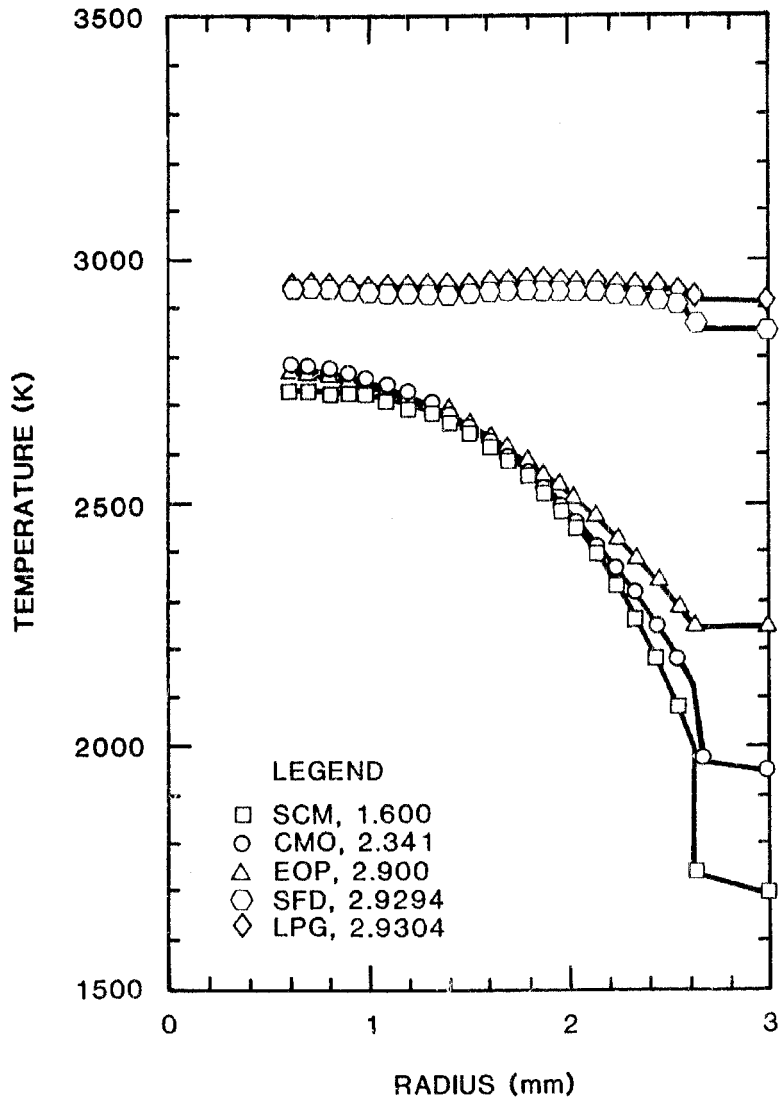


Figure 5-17 HRR-3 radial-temperature profiles.

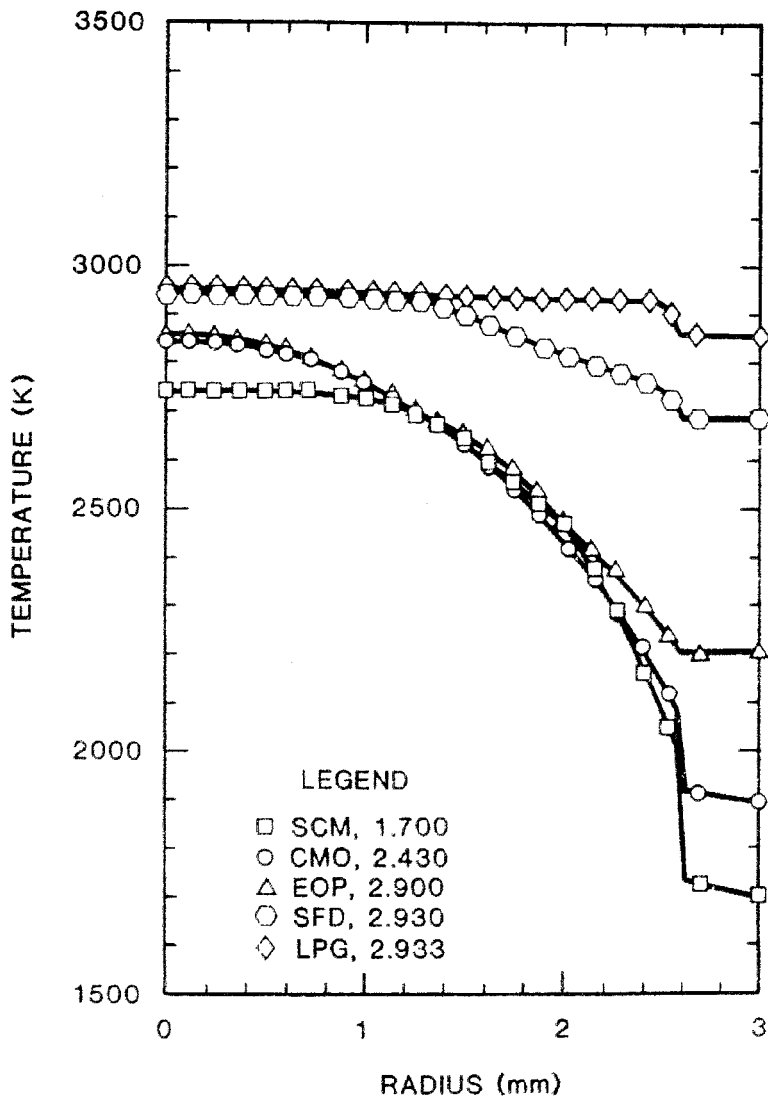
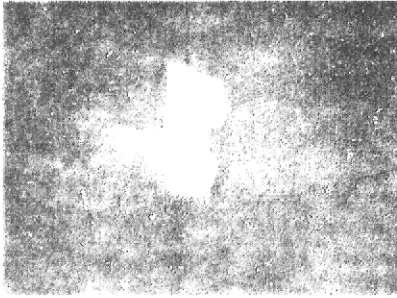
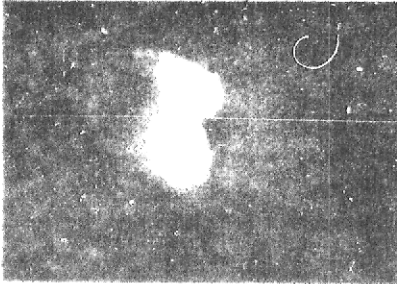


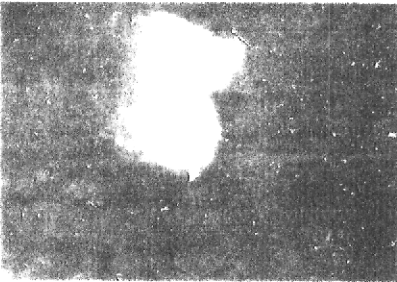
Figure 5-18 HRR-5 radial-temperature profiles.



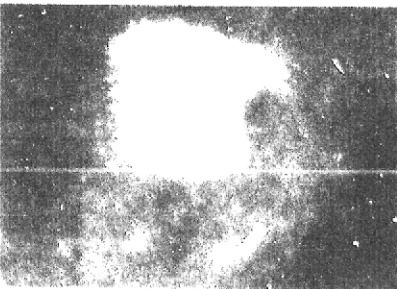
- a. 50% clad meltoff (50% CMO),
t = 2.950 s.



- b. Fuel sputtering,
t = 2.956 s.

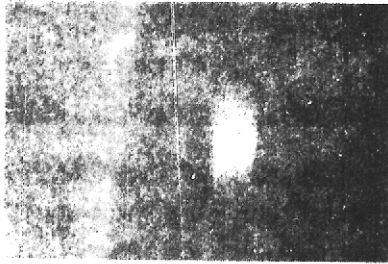


- c. Start of fuel disruption (SFD),
t = 2.959 s.

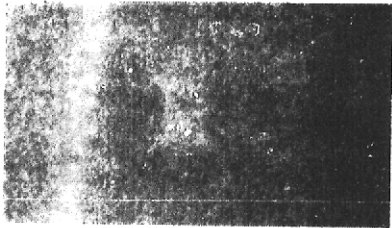


- d. Loss of pin geometry (LPG),
t = 2.962 s.

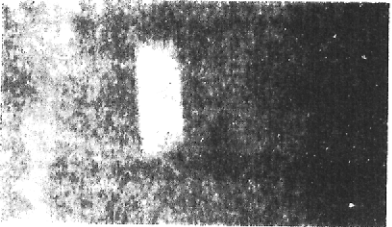
Figure 5-19 Selected frames from motion-picture film (HRR-2).



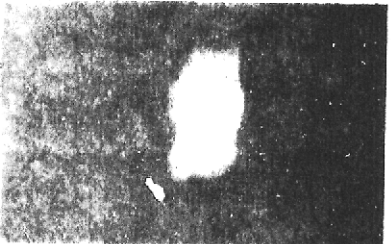
- a. 90% clad meltoff (90% CMO),
t = 2.3410 s.



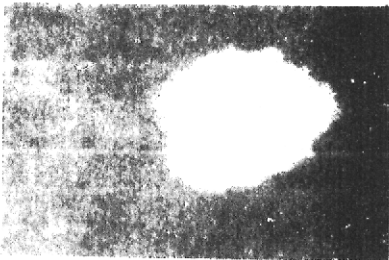
- b. Start of second pulse,
t = 2.9214 s.



- c. Prior to start of fuel disruption,
t = 2.9264 s.

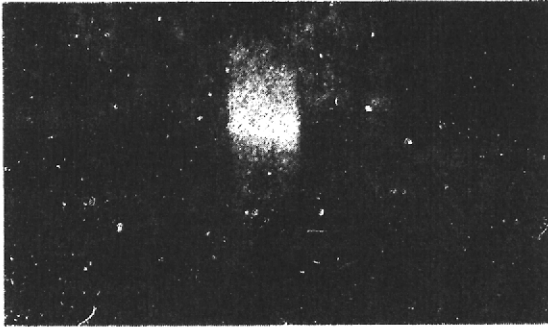


- d. Start of fuel disruption (SFD),
t = 2.9294 s.

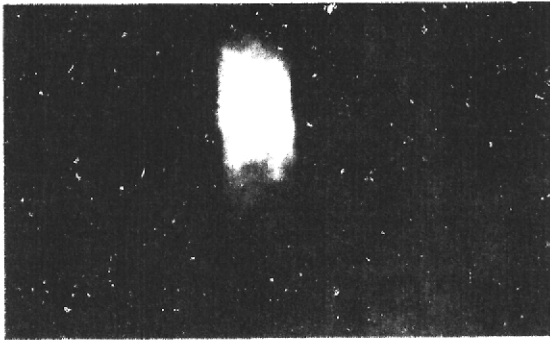


- e. Loss of pin geometry (LPG),
t = 2.9304 s.

Selected frames from motion-picture film (HRR-3).



- a. 90% clad meltoff (90% CMO),
t = 2.430 s.



- b. Start of fuel disruption (SFD),
t = 2.930 s.



- c. Loss of pin geometry (LPG),
t = 2.933 s.

Figure 5-21 Selected frames from motion-picture film (HRR-5).

only real difference was in the fuel-expansion rates at SFD. Figures 5-22 through 5-24 show the measured fuel expansion as a function of time for the irradiated-fuel experiments. In each case, the expansion rates (particle velocities) went from zero to 4 or 5 m/s within 1 ms of the start of fuel disruption. These velocities were about four times larger than the observed expansion rates in the fresh-fuel experiment HRR-6 (see Figure 5-11).

Although the qualitative appearance of the fuel disruption was very similar for fresh- and irradiated-fuel experiments, the timing of SFD was consistently earlier in the irradiated-fuel cases. The calculated radial temperature profiles in Figures 5-16 through 5-18 show that, within the ± 1 -ms timing uncertainty, the time of SFD coincided roughly with the onset of fuel melting. At the time of SFD, fuel-surface temperatures were about 2700 K, the areal melt fraction ranged from 0 to 45%, and the total melt fraction (fractional enthalpy through the heat of fusion, mass average) ranged from 0 to 5%. These values are summarized in Table 5-4. In an absolute sense, the uncertainties in these calculated melt fractions were $\pm 33\%$.

Table 5-4 HRR fuel-melt-fraction summary at time of disruption

| | HRR-6 | HRR-2 | HRR-3 | HRR-5 |
|-----------------------------|--------|-------|--------|-------|
| <u>SFD</u> | | | | |
| Time (s) | 2.9255 | 2.959 | 2.9294 | 2.930 |
| Areal melt fraction (%) | 99 | 0 | 44 | 27 |
| Enthalpy melt fraction* (%) | 12 | 0 | 5 | 4 |
| <u>LPG</u> | | | | |
| Time (s) | 2.9285 | 2.962 | 2.9304 | 2.933 |
| Areal melt fraction (%) | 100 | 20 | 96 | 90 |
| Enthalpy melt fraction (%) | 76 | 1 | 12 | 14 |

* Absolute uncertainty of $\pm 38\%$, relative uncertainty of $\pm 14\%$.

The peak temperatures at the start of fuel disruption were only slightly above the solidus, and the peak fuel-vapor pressures were less than 0.004 MPa. Fuel-vapor pressure could thus be ruled out as the dispersal mechanism. This is more clearly shown in Table 5-5, which gives the times of SFD in comparison with the times at which the peak fuel temperature reached the 0.03 MPa boiling point (~ 3200 K) and the 0.1 MPa boiling point (~ 3500 K). For the irradiated-fuel

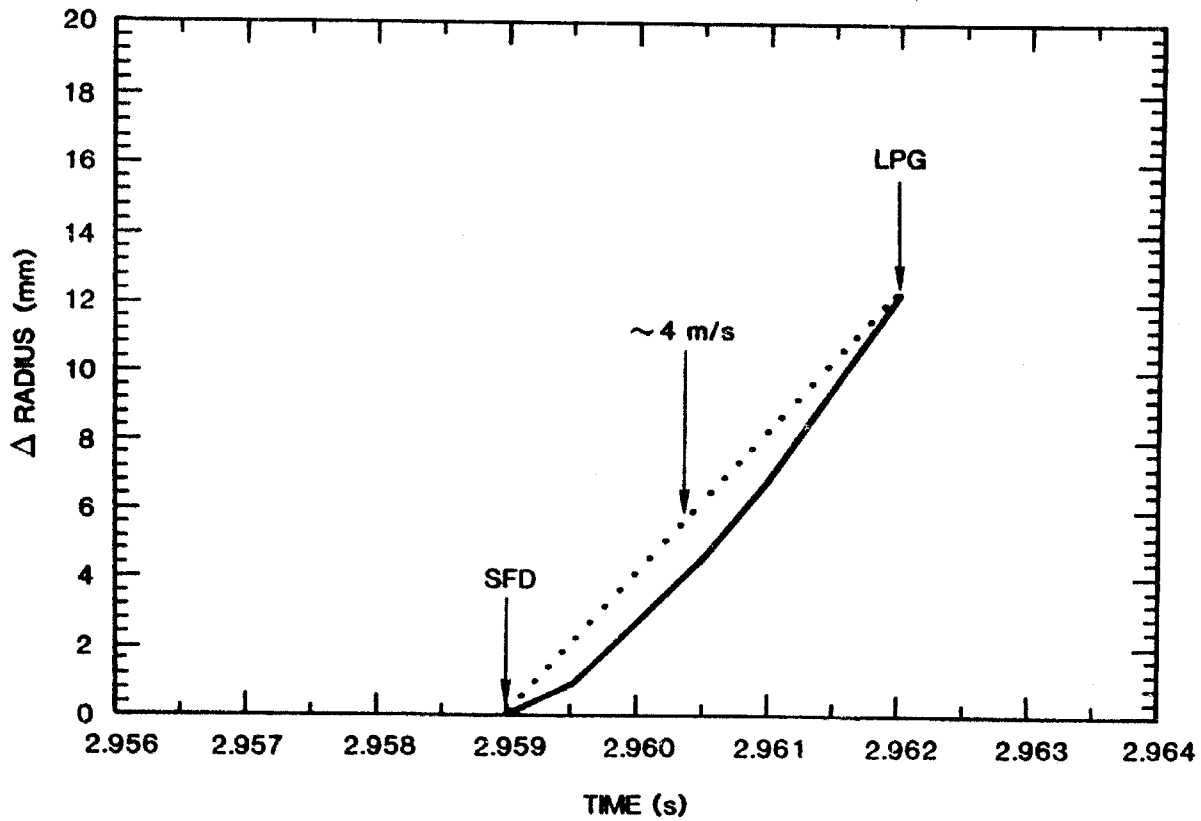


Figure 5-22 Fuel-expansion data for HRR-2.

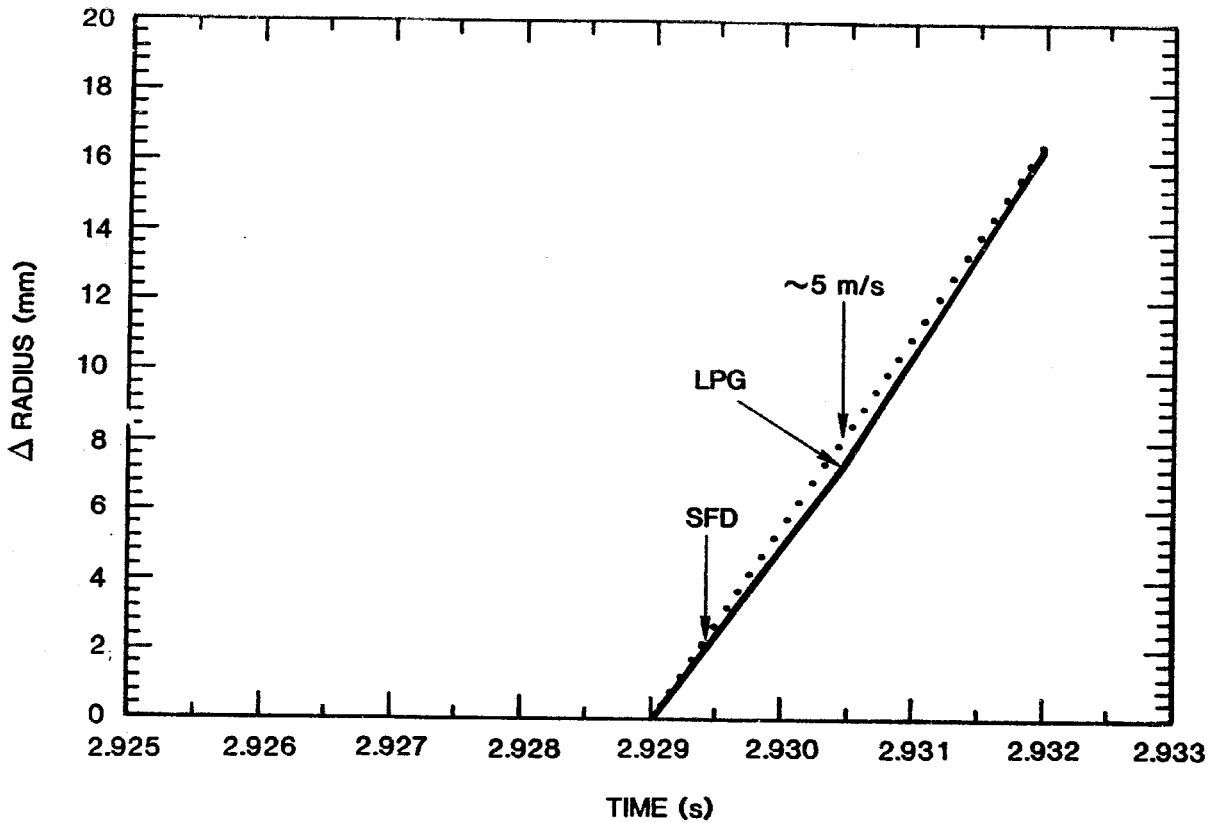


Figure 5-23 Fuel-expansion data for HRR-3.

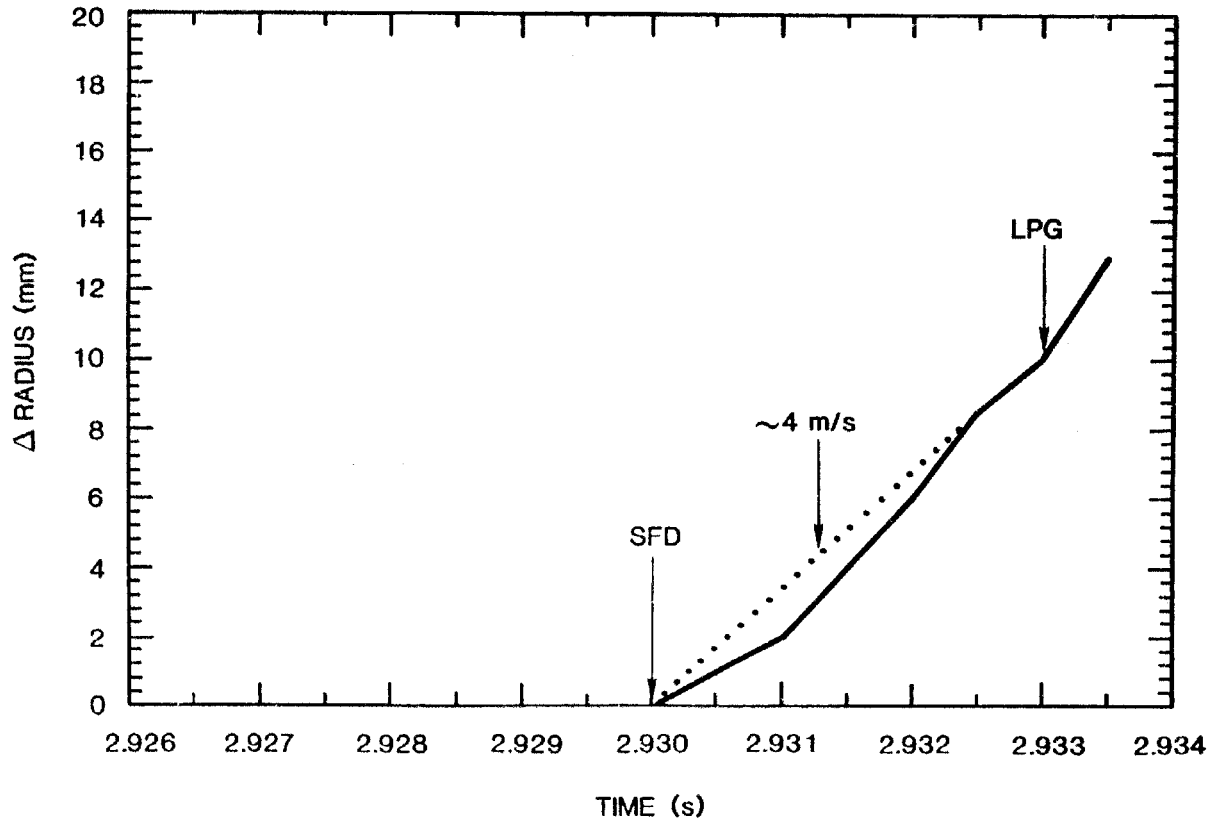


Figure 5-24 Fuel-expansion data for HRR-5.

Table 5-5 Time of fuel-vapor-pressure generation in HRR experiments

| | HRR-6 | HRR-2 | HRR-3 | HRR-5 |
|-----------------------------|--------|-------|--------|--------|
| Time of SFD (s) | 2.9255 | 2.959 | 2.9294 | 2.930 |
| Time of LPG (s) | 2.9285 | 2.962 | 2.9304 | 2.933 |
| Time when vapor pressure | | | | |
| = 0.03 MPa (s) | 2.929 | 2.968 | 2.9365 | 2.9415 |
| = 0.1 MPa (s) | 2.931 | 2.970 | 2.939 | 2.9445 |

experiments, there was a margin of ~ 7 to 10 ms between SFD and the start of rapid fuel vaporization (boiling). This margin was much larger than the \pm 2-ms timing uncertainty in the analysis.

As was mentioned above, the initial rate of fuel expansion was much higher in the irradiated-fuel experiments than in HRR-6. Further, it was not possible to discern a noticeable change in the fuel-expansion rates as was seen in the fresh-fuel HRR-6 experiment. However, long after LPG, when the expanding fuel had filled the entire view field, the character of the fuel seemed to change from discrete (though small) particles to a fog. This occurred near the time of fuel boiling in each experiment.

There are several important conclusions that can be drawn from these results:

- There seemed to be no difference in the observed fuel disruption between high- and low-power microstructures (HRR-3 versus HRR-5).
- There seemed to be no difference in the observed fuel disruption between preheat temperatures of 2300 K and 2500 K (HRR-2 versus HRR-3).
- There was no evidence for fuel disruption below fuel temperatures of ~ 2300 K (although the fuel may have fragmented prior to disruption).
- The irradiated fuel disrupted earlier than the fresh fuel, but in a qualitatively similar manner (HRR-2 versus HRR-6).

Based on these analyses, it appears that that observed disruption coincided very nearly with fuel melting (or near melting) in the irradiated-fuel samples. Solid-state disruption, as predicted by the

TIGRS pretest calculations, was not observed. Solid-state disruption may have occurred, but only when the center of the pin was starting to melt.

5.2.3 Comparisons between Fresh- and Irradiated-Fuel Experiments

The differences between the fresh- and irradiated-fuel experiments have been briefly discussed in the previous section. These important differences and similarities are again summarized herein to aid in the interpretation of the results. Table 5-6 summarizes the major observations and analysis for all the HRR experiments.

The disruption process was qualitatively very similar for both the fresh- and irradiated-fuel experiments; it appeared as a rapid gas-driven expansion of very fine particles. In all cases, disruption occurred well before significant fuel vapor pressure was generated. If this observed disruption proves to be axially dispersive, it would be an important potential source of reduction in work-energy release for prompt-burst disassembly accidents, especially in end-of-equilibrium-cycle (EOEC) cores. Further, if the observed early dispersal in the fresh fuel can be demonstrated to be prototypic, this reduction in work-energy release could be extended to beginning-of-life (BOL) cores as well.

The major difference between fresh and irradiated-experiments was the state of the fuel at the time of disruption. This was most clearly seen in the melt fraction at the start of fuel disruption. The fresh fuel was nearly 100% molten, whereas the irradiated fuel had a lower melt fraction (average ~ 40%). This difference was even more pronounced, since the melt temperature for the fresh fuel (3021 K) was higher than for the irradiated fuel (2960 K). Thus, given the same power transient, irradiated fuel disrupted earlier. This was consistent with the expected result that fission gas in the irradiated fuel contributed to the earlier disruption.

Fresh and irradiated fuels also displayed differences in the initial expansion rates (i.e., the velocity of the particles at the start of fuel disruption). For fresh fuel, this velocity was near 1.25 ± 0.2 m/s; for the irradiated fuel, this rate was near 5.0 ± 0.2 m/s. Again, this difference is thought to be due to the presence of fission products in the irradiated fuel.

A further difference observed between fresh and irradiated fuel was the swelling of fresh fuel, whereas the irradiated fuel experienced little or no swelling. This phenomenon probably occurred because the irradiated fuel disrupted earlier, leaving little or no time for swelling to occur. Evidence for this reasoning is seen in the state of the fuel at the time of swelling in HRR-6 and at the time of disruption in the irradiated-fuel experiments. The fresh fuel started swelling at a significant rate when the fuel-surface temperature reached 2700 to 2800 K. However, when these conditions were reached in the irradiated fuel, disruption occurred (suggesting a larger internal driving pressure).

Table 5-6 Summary of observations for high-ramp-rate fuel-disruption experiments

| Observation | HRR-6 | HRR-2 | HRR-3 | HRR-5 |
|--|--------|-----------|-----------|----------|
| Fuel Characteristics | | | | |
| Fuel Type | FE-094 | PNL 11-18 | PNL 11-18 | PNL 9-44 |
| Sintered Density (10^3 kg/m ³) | 10.0 | 9.96 | 9.96 | 9.88 |
| Enrichment (%) | 70.3 | 67.7 | 67.7 | 40 |
| Burnup (atom percent) | 0 | 4.67 | 4.61 | 4.75 |
| Linear Heat Rating (kW/m) | -- | 33.3 | 32.9 | 15.9 |
| Event Times (s) | | | | |
| CMO | 2.479 | 2.950* | 2.341 | 2.430 |
| FS | 2.9225 | † | † | † |
| SFD | 2.9255 | 2.959 | 2.9294 | 2.930 |
| LPG | 2.9285 | 2.962 | 2.9304 | 2.933 |
| Melt Fraction at SFD (%) | | | | |
| Areal | 99 | 0 | 44 | 27 |
| Enthalpy | 12 | 0 | 5 | 4 |
| Linear Expansion Rate (m/s \pm .2 m/s) | | | | |
| | 1.25 | 5.0 | 5.0 | 4.5 |
| Time (s) at which | | | | |
| Fuel Vapor Pressure = .03 MPa | 2.929 | 2.968 | 2.9365 | 2.9415 |
| Fuel Vapor Pressure = .1 MPa | 2.931 | 2.970 | 2.939 | 2.9445 |
| Reactor Conditions | | | | |
| Preheat Temp (K) | 2320 | 2296 | 2478 | 2480 |
| Preheat Time (s) | 2.5 | 2.5 | 2.5 | 2.5 |
| Temp Ramp at SFD (K/ms) | 90 | 60 | 50 | 45 |

* 50% CMO.

† No significant fuel swelling.

An important objective of the HRR experiments was to determine the source and magnitude of the forces causing the disruption. Since fuel-vapor pressure can be excluded as the initial cause of fuel disruption for both fresh and irradiated fuels, other causes must be considered. The other possible sources are molten-fuel expansion, fission products (especially the gases), and impurity gases. Each of these three factors is likely to play a role.

In the fresh-fuel HRR-6 experiment, only molten-fuel expansion and impurity gases* can be considered as candidate disruptive mechanisms. A detailed analysis of the relative magnitude of these two sources and their interdependence has not been performed, but some qualitative observations can be made. At the time of SFD in HRR-6, the radially averaged melt fraction (fractional enthalpy through the heat of fusion) was only about 10%, and the peak local melt fraction was only 35%. Since the fresh fuel had an as-fabricated porosity of 12%, and the peak volume expansion associated with complete melting was ~ 10% [41], it is unlikely that the volume expansion associated with only 35% peak melting could cause disruption. Thus, impurity gases probably constitute the dominant disruption mechanism.

Other experimental evidence also indicated that the disruption was caused by gases. The films, as well as the photos shown in Figure 5-7, showed the emission of a gaseous halo around the fuel prior to disruption. This gas evolution might be related to the early disruption in the fresh-fuel experiment.

If impurity gases caused the disruption, then what were the gases and under what mechanisms did they operate? Two possible gases are currently under consideration. The first possibility is helium gas. The fuel used in the HRR-6 experiments was fabricated at least 15 years ago, so sufficient time had elapsed to allow the alpha decay of Pu-240 to generate helium in the mixed-oxide lattice. It is estimated that the maximum concentration of helium was 3.8×10^{24} atoms/m³.

The other impurity gas that might have caused the disruption is CO.[42] The mixed oxide fuel was originally fabricated with a carbon wax binder. Most of the carbon escaped in the sintering process, but some remained. The fabrication specifications indicate that this was less than 1.12×10^{24} atoms/m³. During normal steady-state irradiation, the carbon remains in the oxide lattice. But during the accident transient, the carbon could chemically react with the oxide to become CO at temperatures greater than 2000 K. If this reaction process was fast enough, then the CO could have pressurized the interior of the fuel and cause it to disrupt. In addition, gases adsorbed during the handling of the pin (water and hydrocarbon vapors) may have also contributed to the observed disruption.

* Impurity gases include contaminants introduced during handling as well as gases that may be inherent or formed from inherent materials included in the fuel at the time of fabrication. Carbon and helium are examples of fabrication impurities.

The helium and CO concentrations given are only estimates (the CO concentration may be higher). However, these concentrations can still be compared to a typical fission-gas concentration (see Section 2.2) of 1.3×10^{26} atoms/m³. Based on this comparison, it would seem that helium and impurity gases (such as CO) play only a minor role, if any, in the disruption of irradiated fuel. Nevertheless, analysis of the impurity gases is needed to better determine the role they play in the HRR experiments and their importance under prototypic transient conditions.

5.3 Postexperiment Fission-Gas Calculations

The postexperiment calculations were similar to the preexperiment calculations, except that they used the actual experiment-temperature histories and were performed with the SANDPIN code rather than the TIGRS code.

The SANDPIN calculations provided a coupled thermal/fission-gas analysis of the HRR experiments. The actual temperature and temperature-gradient histories were used in the analyses. The best-estimate radial distributions of fission-gas content, as described in Appendix A, were used. Gas-bubble-dynamics calculations and predictions of fuel cracking were made as a function of radial position in the fuel-pellet stack.

The actual fission-gas-dynamics calculations in SANDPIN were similar to those in TIGRS. Primary differences between the two codes lay in the treatment of grain-boundary gas. SANDPIN differentiated between interlinked and closed-grain boundary porosity as well as between the initial intergranular gas (typically in large bubbles) and the intergranular gas that accumulates during a transient as a result of intragranular release. The cracking criteria used in SANDPIN were the same as those in TIGRS. However, the different treatment of intergranular gas led to different predictions of intergranular cracking.

The results of the SANDPIN fission-gas calculations for HRR-2, -3, and -5 are shown in Table 5-7. Shown are the predicted times of solid-state disruption along with the observed disruption times. For HRR-3 and HRR-5, disruption was predicted to occur 3 to 5 ms before the observed disruption. For HRR-2, disruption was not predicted to occur, although the ratio of the energy available to the energy needed to cause cracking (the total-energy criterion in TIGRS and SANDPIN) reached a value of 0.94. This energy fraction was very close to 1.0, especially when one considers uncertainties in model parameters such as the incipient crack size. In all cases, the predicted disruption was intergranular and involved the outer 15 to 20% of the fuel pellet.

Also shown in Table 5-7 are the predicted disruption times for experiments HRR-2, -4, and -5 when a $\pm 30\%$ uncertainty in initial gas content is considered. As can be seen from these results, for the HRR transients, predictions of fission-gas-induced fuel cracking were sensitive to the assumed gas content. When a 30%-lower-than-nominal gas content was assumed, cracking was not predicted to occur

Table 5-7 Comparison of measured and predicted fuel-disruption times for experiments HRR-2, -3, and -5

| | HRR-2 | HRR-3 | HRR-5 |
|---|--------|--------|--------|
| Measured Disruption Time (s) | 2.959 | 2.9294 | 2.930 |
| Calculated Disruption Time (s) With Gas Content | | | |
| nominal | (.94)* | 2.9246 | 2.9297 |
| +30% | 2.9597 | 2.913 | 2.9197 |
| -30% | (.76)* | (.94)* | (.88)* |

* No disruption predicted -- value in parentheses is peak of available-to-required-energy ratio at measured time of disruption.

in any of the three experiments. For the 30%-higher gas-content calculations, cracking was predicted in all cases. In fact, for HRR-3 and HRR-5, cracking was then predicted near the start of the fast heating ramp.

Based on the analysis presented above we must include the possibility of some solid state fuel disruption occurring in the gas bearing fuel. However, the thermal analysis presented in Section 5.2.2 showed that fuel disruption occurred near the time of fuel melting in all experiments. Thus it appears that if solid-state disruption did occur it coincided with the onset of fuel melting. Because the fission gas bubbles are highly over pressurized when fuel melting occurs (i.e. they are not in hydrostatic equilibrium with the fuel matrix), they will expand causing the fuel to swell or disrupt. It is this mechanism that we feel is primarily responsible for the disruption since it has a much stronger potential for energy release.

6. SUMMARY AND CONCLUSIONS

The four fuel-disruption experiments in the HRR series, described in this document, have provided valuable data concerning the behavior of both fresh and irradiated fuel under rapid-heating conditions characteristic of a prompt-burst disassembly. The major experimental results can be summarized as follows:

- The initial disruption occurred significantly prior to fuel-vapor-pressure generation for both fresh and irradiated fuel samples.
- In the fresh-fuel experiment, fuel disruption was characterized by rapid fuel swelling (starting when the fuel-surface temperature reached 2700 to 2800 K) followed by a rapid spray-like dispersal of the fuel (when the areal melt fraction reached ~ 100%).
- In the irradiated-fuel experiments, fuel disruption was simply a rapid spray-like dispersal that occurred when the fuel-surface temperature reached 2700 to 2800 K. At this time the peak fuel temperatures were near the solidus temperature.
- The apparent character and timing of the dispersal in the irradiated-fuel experiments was insensitive to fuel microstructure and steady-state operating (preheat) temperature.
- The dispersal in the irradiated-fuel experiments was more energetic (more rapid) than in the fresh-fuel experiments.
- Disruption of the irradiated fuel significantly prior to fuel melting was not observed.

Based on these observations and the preliminary thermal and fission-gas analyses done to date, the following interpretations have been made concerning the cause of the disruption:

- The most likely cause of the observed early fuel disruption in the fresh-fuel experiment was impurity gas driven expansion occurring at the onset of fuel melting. This was probably augmented by the volume expansion upon fuel melting.
- The most likely cause of the observed early fuel disruption in the irradiated-fuel experiments was fission products gas driven expansion occurring at the onset of fuel melting. This may also be augmented by impurity gases and volume expansion upon fuel melting, and possible solid-state disruption in the outer gas bearing regions of the fuel.

Further analysis is continuing to quantify the dispersive forces described above. Of primary importance is the evaluation of nonprototypic features in the HRR experiments to determine whether these results are applicable to actual reactor transients. One potential nonprototypic feature that must be examined is the impurity-gas concentrations in the HRR fuel samples, compared to those expected in prototypic (clean) reactor fuel.

If these observations and conclusions can be generalized to actual reactor-accident transients, it must still be demonstrated that the observed disruption, together with the streaming coolant and steel vapor, provides the negative reactivity feedback needed to terminate the accident excursion. Thus, it must be demonstrated that, in a prototypic bundle geometry, the type of violent radial fuel dispersal seen in the HRR experiments leads to axial dispersal of fuel away from the high-worth regions of the core. Experiment programs designed to investigate this axial dispersal are currently in the planning stages at SNLA. These experiments will be similar to the fuel-disruption-type experiments but will use single pin and multi-pin bundles in a flowing gas-cooled environment.

REFERENCES

1. Nicholson, R. B. and J. F. Jackson, "Particle Voiding and Fission Product Gas in LMFBR Disassembly Calculations," Trans Amer Nucl Soc 14:737, 1971.
2. Teague, H. J. and D. J. Mather, "Factors Limiting Prompt-Critical Excursions in Irradiated Fast Reactor Cores," Nucl Safety 14(3):201-205, May-June 1973.
3. Worledge, D. H. and G. L. Cano, "Study of the Dispersive Potential of Irradiated Fuel Using In-Core Experiments," Proc. Intl. Meeting on Fast Reactor Safety Technology, Seattle, WA, August 1979.
4. Worledge, D. H., "Fuel Fragmentation by Fission Gases During Rapid Heating," SAND80-0328 (Albuquerque, NM: Sandia National Laboratories, 1980).
5. Technical Highlights/Administrative Report for the Nuclear Regulatory Commission (NRC)--Advanced Reactor Safety Research Program, Sandia National Laboratories, March 1981.
6. Williams, D. C., et al, "LMFBR Accident Delineation Study--Phase I Final Report," SAND80-1267 (Albuquerque, NM: Sandia National Laboratories, 1980).
7. Bethe, H. A. and J. H. Tait, "An Estimate of the Order of Magnitude of the Explosion When the Core of a Fast Reactor Collapses," United Kingdom Atomic Energy Authority, RHM(56)/113, April 1956.
8. Sha, W. et al, "Two-Dimensional Fast-Reactor Disassembly Analysis with Space-Time Kinetics," Proc. Conf. New Developments in Reactor Mathematics and Applications, Idaho Falls, ID, March 1971.
9. Brook, A. J., "Some Preliminary Considerations Relating to an Equation of State for Irradiated Nuclear Fuel," Nucl Safety 13(6):467-477, November-December 1972.
10. Walker, S. P., "The Inclusion of Fission Gas Pressures in Disassembly Calculations: A Computational Model with Numerical Results Obtained," SRD R167, Safety and Reliability Directorate, Warrington, Cheshire, U.K., December 1979.
11. Gruber, E. E., "Calculation of Transient Fission-Gas Release from Oxide Fuels," Argonne National Laboratory report ANL-8143, November 1974.

12. Rest, J., "GRASS-SST: A Comprehensive, Mechanistic Model for the Prediction of Fission-Gas Behavior in UO_2 Base Fuels during Steady-State and Transient Conditions," Argonne National Laboratory report ANL-78-53, June 1978.
13. Ostensen, R. W., "FISGAS--A Code for Fission-Gas Migration and Fuel Swelling in an LMFBR Accident," SAND78-1790 (Albuquerque, NM: Sandia National Laboratories, 1979).
14. Griesmeyer, J. M. and D. Okrent, "A New Model for Nonequilibrium Fission-Gas Behavior," Trans Amer Nucl Soc 27:322, 1977.
15. Matthews, J. R. and M. H. Wood, "Modelling the Transient Behaviour of Fission Gas," J Nucl Materials 84:125-136, 1979.
16. Ostensen, R. W., "Comparison of FISGAS Swelling and Gas Release Predictions with Experiment," Proc. Specialists' Workshop on Predictive Analysis of Material Motion in LMFBR Safety Experiments, Los Alamos, NM, March 13-15, 1979.
17. Dimelfi, R. J. and L. W. Deitrich, "The Effect of Grain Boundary Fission Gas on Transient Fuel Behavior," Nucl Tech 43:, May 1979.
18. Bandyopadhyay, G., "Response of Oxide Fuel to Simulated Thermal Transients," Nucl Tech 41:349-358, Mid-December 1978.
19. Randklev, E. H. and C. A. Hinman, "Ex-Reactor Transient Fission Gas Release Studies: Fuel Pins PNL 10-50 and PNL 10-55," Hanford Engineering Development Laboratory report HEDL-TME 79-52, September 1980.
20. Gruber, E. E. et al, "Analysis of Fuel Dispersal in Direct Electrical Heating Experiments," Proc. Specialists' Workshop on Predictive Analysis of Material Motion in LMFBR Safety Experiments, Los Alamos, NM (March 13-15, 1979).
21. Rothman, A. B. et al, "TREAT Experiments with Irradiated Fuel Simulating Hypothetical Loss-of-Flow Accidents in Large LMFBRs," Proc. Intl. Meeting on Fast Reactor Safety Technology, Seattle, WA, August 1979.
22. Simms, R. et al, "TREAT Experimental Data Base Regarding Fuel Dispersals in LMFBR Loss-of-Flow Accidents," ANS/ENS Topical Meeting on Reactor Safety Aspects of Fuel Behavior, Sun Valley, ID, August 1981.
23. McTaggart, M. H. and J. R. Findlay, "Progress Report on the VIPER Measurements of Fission Product Pressure Generation," AWRE/44/96/3, SRD R106, AWRE, Aldermaston, Berkshire, U.K., January 1978.
24. Cano, G. L. et al, "Visual Investigation of Reactor Fuels Response to Simulated LOF Heating Conditions, First Series," SAND79-0940 (Albuquerque, NM: Sandia National Laboratories, 1979).

25. Chidester, K. M., K. P. Keenan and W. E. Warden, "Fabrication Data Package on Fuel Pins for EBR-II Subassemblies PNL 9, 10, 11," Hanford Engineering Development Laboratory report HELD-TME 72-18, May 1972.
26. Scott, J. H. et al, "Preliminary Data Report; Post-Irradiation Examination of Fuel Pins PNL 10-23 and PNL 10-63," Hanford Engineering Development Laboratory report HEDL-TME 74-23, May 1974.
27. Leggett, R. D. (Hanford Engineering Development Laboratory), private communication, May 20, 1977.
28. Dutt, D. S. and R. D. Baker, "SIEX, A Correlated Code for the Prediction of Liquid Metal Fast Breeder Reactor (LMFBR) Fuel Thermal Performance," Hanford Engineering Development Laboratory report HEDL-TME 74-55, June 1975.
29. Dutt, D. S. et al, "A Correlated Fission-Gas Release Model for Fast Reactor Fuels," Trans Amer Nucl Soc 15:198, 1972.
30. Randklev, E. H., "Radial Distribution of Retained Fission Gas in Irradiated Mixed-Oxide Fuel," Trans Amer Nucl Soc 28:234, June 1978.
31. Randklev, E. H. et al, "Fission Gas Behavior in Mixed-Oxide Fuel During Transient Overpower," Proc. Intl. Meeting on Fast Reactor Safety Technology, Seattle, WA, August 1979.
32. Graczyk, D. G. et al, "A Laser Microsampling Method for Determination of Retained Fission Gas in Irradiated Nuclear Fuels," Argonne National Laboratory report ANL 79-86, October 1979.
33. Wang, W. L. et al, "Transient Fission-Gas Behavior: Experimental and Analytical Results," Trans Amer Nucl Soc, 28:240-241.
34. Preston-Thomas, H., ed., Temperature, Its Measurement and Control in Science and Industry, Vol. 4, part 1, American Institute of Physics, p. 503, 1972.
35. Advanced Reactor Safety Research Quarterly Report July-September 1981, SAND81-1529 (Albuquerque, NM: Sandia National Laboratories, 1981).
36. Peterson, T. F., "TAC2D--A General Purpose Two-Dimensional Heat Transfer Code--User's Manual," GA8868, Gulf General Atomic, San Diego, CA, 1969.
37. Leibowitz, L. et al, "Properties for LMFBR Safety Analysis," Argonne National Laboratory report ANL-CEN-RSD-76-1, April 1976.
38. Baker, R. B., "Calibration of a Fuel-to-Cladding Gap Conductance Model for Fast Reactor Fuel Pins," Hanford Engineering Development Laboratory report HEDL-TSME 77-85, May 1978.

39. Browning, P., "On the Relative Importance of the Electronic and Radiative Contributions to the Thermal Conductivity of Uranium Dioxide," J Nucl Materials 92:33-38, 1980.
40. Slagle, D. D., "Creep of UO₂ at 2500°C," Hanford Engineering Development Laboratory report HEDL-SA-1079, 1977.
41. SANDPIN (to be published).
42. Breitung, W. M., "Contamination Control in Sandia Equation-of-State Experiments," SAND80-1277 (Albuquerque, NM: Sandia National Laboratories, 1980).

APPENDIX A

ASSUMED FUEL FISSION-GAS DISTRIBUTIONS

Early calculations of fission-gas behavior used fission-gas concentrations derived from the Dutt correlation.[29] Recent experimental work by Randklev and by Bandyopadhyay has shown that neither the total (integrated over fuel radius) gas content nor the radial distribution is described very well by the Dutt correlation.[30,31] This lack of agreement with the Dutt correlation is also seen in the results of theoretical descriptions of steady-state gas release.[33] The published work of Randklev has been used to describe the best-estimate distribution of retained inter- and intragranular gas. These distributions are described below.

Randklev's work indicates that the radial distribution of retained intragranular gas (shown in Figure A-1) is

- 1) flat over the outer $\sim 300 \mu\text{m}$ of the fuel pellet,
- 2) drops off rapidly over the next $\sim 300 \mu\text{m}$ of the pellet, and
- 3) is again relatively flat over the inner $\sim 1900 \mu\text{m}$.

Most significantly, the radial distribution as shown in Figure A-1 appears to be essentially independent of fuel microstructure and local linear heat rating. Furthermore, the peak concentration in the outer part of the fuel, C_1 , appears to be independent of local linear heat rating and a function only of local fuel burnup. Thus, PNL 9, PNL 10, and PNL 11 fuel pins of similar burnup have essentially identical radial distributions of retained intragranular gas.

Randklev's work also indicates that a significant amount of the retained gas is located intergranularly. He states that "recent measurements of retained gas . . . indicated ~ 20 to 25 percent of the retained gas was located intergranularly." [30] Measurements of radial distributions of retained intergranular gas have not been made. Randklev merely states that the intergranular gas " . . . occurs primarily in the region radially inward of $\sim 0.75 r_0$ and most probably between $\sim 0.75 r_0$ and $0.25 r_0$, where r_0 is the [outer] fuel radius." [30] Based on these statements, it is assumed as a first approximation that the radial distribution of retained intergranular gas is as shown in Figure A-2.

There is no accompanying data on the axial distribution of retained intergranular and intragranular fission-gas concentrations in the PNL 9, PNL 10, and PNL 11 pins. The fuel pins used in the HRR experiments have peak burnups on the order of 4 to 6 atom percent. For this range of burnups, the Dutt correlation predicts very little variation in

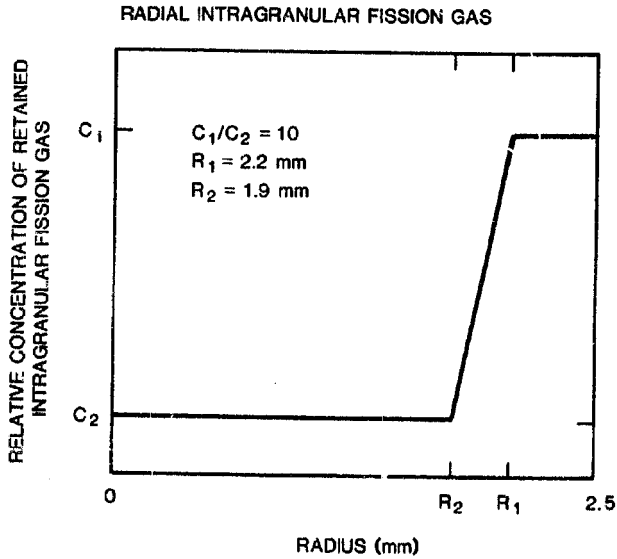


Figure A-1 Initial intragranular fission-gas concentration (based on Randklev's work).

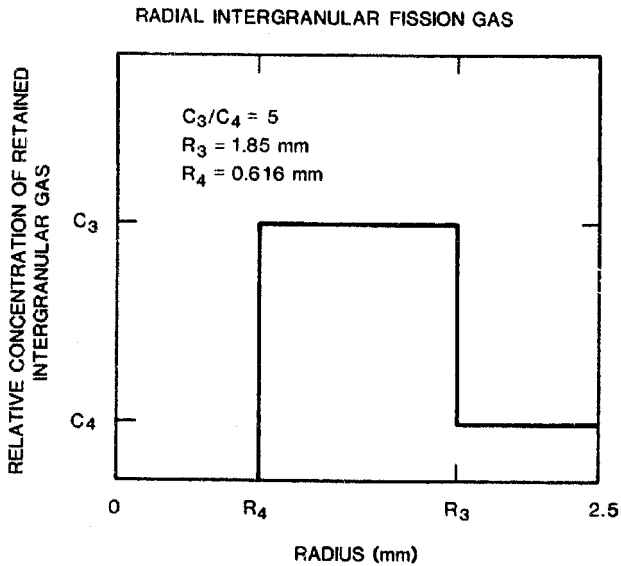


Figure A-2 Initial intergranular fission-gas concentration (based on Randklev's work).

gas concentration. Since the peak-to-average burnup ratio in the PNL pins is only on the order of 1.1, it is assumed as a first approximation that there is no axial variation in the retained fission-gas concentrations in the PNL 9, PNL 10, and PNL 11 pins. This approximation will be revised as better data become available.

Using the radial distributions given in Figures A-1 and A-2, the assumption of no axial variation in these distributions, and a 25/75 split between intergranular versus intragranular gas, the concentrations C_1 , C_2 , C_3 , and C_4 can be calculated knowing the total amount of retained gas in the pin. This quantity is normally backcalculated from the total amount of gas generated (simply a function of burnup) and the amount of gas released to the fission-gas plenum. Since the amount of plenum gas in the particular PNL pins used in the HRR experiments is not known, the average quantities of retained gas given by Randklev are used in analysis. He quoted average gas-retention values of 22.8 cc, 21.7 cc, and 23.4 cc (at STP) for the PNL 9, PNL 10, and PNL 11 pins, respectively. Using these values for total gas retention, the intragranular concentrations, C_1 and C_2 , and the intergranular concentrations, C_3 and C_4 , can be calculated. These concentrations are listed in Table A-1, along with the concentration, C_0 , that would be calculated using the Dutt correlation.

Table A-1 Gas concentration* summary

| Fuel Pin | Dutt Correlation | Intragranular Concentrations | | Intergranular Concentrations | |
|----------|------------------|------------------------------|-------|------------------------------|-------|
| | C_0 | C_1 | C_2 | C_3 | C_4 |
| PNL-9 | 155 | 146 | 14.6 | 35.8 | 7.15 |
| PNL-10 | 154 | 139 | 13.9 | 34.0 | 6.81 |
| PNL-11 | 147 | 150 | 13.0 | 36.7 | 7.34 |

* All concentrations in 10^{24} atoms/ m^3 at the axial midplane.

DISTRIBUTION:

Division of Technical Information
and Document Control
NRC Distribution Contractor
U.S. Nuclear Regulatory Commission
15700 Crabbs Branch Way
Rockville, MD 20850
(250 copies for R7)

U.S. Nuclear Regulatory Commission (7)
Division of Accident Evaluation
Office of Nuclear Regulatory Research
Washington, DC 20555
Attn: D. F. Ross
O. E. Bassett
C. N. Kelber
G. Marino
R. T. Curtis
R. W. Wright
P. Wood

U.S. Nuclear Regulatory Commission
Office of Nuclear Reactor Research
Clinch River Breeder Reactor Program Office
Washington, DC 20555
Attn: C. Allen

U.S. Department of Energy
Office of Nuclear Safety Coordination
Washington, DC 20545
Attn: R. W. Barber

U.S. Department of Energy (2)
Albuquerque Operations Office
P. O. Box 5400
Albuquerque, NM 87185
Attn: J. R. Roeder, Director
Operational Safety Division
D. L. Krenz, Director
Energy Technologies Division
For: C. B. Quinn
R. N. Holton

Los Alamos National Laboratory
P. O. Box 1663
Los Alamos, NM 87145
Attn: C. R. Bell, Q-7

DISTRIBUTION (Continued)

**Technology Management Center
Argonne National Laboratory
Building 207
9700 S. Cass Avenue
Argonne, IL 60439
Attn: L. Baker**

**Department of Nuclear Energy
Building 820
Brookhaven National Laboratory
Upton, NY 11973
Attn: T. Ginsberg**

**Argonne National Laboratory (9)
9700 South Cass Avenue
Argonne, IL 60439
Attn: B. W. Spencer
 J. J. Sienicki
 J. M. Kramer
 T. E. Kraft (3)
 G. Feuske
 L. W. Deitrich
 R. Demelfi**

**Dr. Carl A. Erdman
Nuclear Engineering Department
Texas A and M University
College Station, TX 77843**

**General Electric Corporation (4)
310 DeGuigne Drive
Sunnyvale, CA 94086
Attn: S. M. Davies, Mgr., LSPB Project
 T. I. Temme, Mgr., Probabilistic
 Risk Assessment
 D. M. Switick, Mgr., Plant Safety
 S. Rhow**

**Fauske and Associates, Inc.
16W070 West 83rd Street
Burr Ridge, IL 60521
Attn: Dr. Michael Grolmes**

DISTRIBUTION (Continued)

Projekt Schneller Brueter (10)
Kernforschungszentrum Karlsruhe GMBH
Postfach 3640
D75 Karlsruhe
West Germany

Attn: Dr. Kessler (2)
Dr. Heusener (2)
Dr. Froelich
Dr. Werle
Dr. Kuhn
Dr. Groetzbach
Dr. Fischer
Dr. Vaeth

UKAEA Safety and Reliability Directorate (5)
Wigshaw Lane
Culcheth
Warrington WA3 4NE
Cheshire
England

Attn: Dr. J. Gittus, Director
Dr. M. J. Hayns
Mr. H. Teague
Dr. R. S. Peckover
Dr. D. McInnes

AERE Harwell
Didcot
Oxfordshire OX11 0RA
England

Attn: Dr. J. R. Matthews,
Theoretical Physics Division

UKAEA (2)
Risley
Warrington WA3 6AT
Cheshire
England
Attn: Dr. B. Cowking, FRDD
Dr. D. Hicks, TRDD

Dr. F. Briscoe
Culham Laboratory
Culham
Abingdon
Oxfordshire OX14 X
England

DISTRIBUTION (Continued)

Mr. C. P. Gratton
Division Head, SESD
Atomic Energy Establishment
Winfrith,
Dorset DTZ 8DH
England

K. S. Norwood
Mail Stop B 12
Building 4500 N
Oak Ridge National Laboratory
P. O. Box X
Oak Ridge, TN 37830

Joint Research Centre (3)
Ispra Establishment
21020 Ispra (Varese)
Italy
Attn: H. Holtbecker
P. Fasoli-Stella
R. Klersy

Power Reactor and Nuclear Fuel (6)
Development Corporation (PNC)
Fast Breeder Reactor Development Project (FBR)
9-13, 1-Chome, Akasaka
Minato-Ku, Tokyo
Japan
Attn: Dr. A. Watanabe
Dr. K. Takahashi
Dr. N. Tanaka (3)
Dr. N. Nonaka

Centre d'Etudes Nucleaires de Cadarache (4)
Boite Postale No. 1
13115 St. Paul lez Durance
France
Attn: A. Meyer-Heine DERS/SIES
J. Cl. Melis DERS/SIES
M. Schwarz DERS/SIES
C. LeRigoleur DRNR/SYTC

DISTRIBUTION (Continued)

1230 J. E. Powell
3141 C. M. Ostrander (5)
3151 W. L. Garner
3461 B. N. Yates
6350 R. M. Jefferson
6400 A. W. Snyder
6410 J. W. Hickman
6420 J. V. Walker
6420 M. Hasti
6420 M. Watkins
6421 T. R. Schmidt
6421 J. T. Hitchcock
6422 D. A. Powers
6422 J. E. Brockmann
6422 R. M. Elrick
6422 A. R. Taig
6423 P. S. Pickard (2)
6423 A. C. Marshall
6423 D. A. McArthur
6423 G. Schumacher
6423 S. A. Wright (5)
6425 W. J. Camp
6425 G. Kayser
6425 P. K. Mast
6425 M. F. Young
6427 M. Berman
6440 D. A. Dahlgren
6442 W. A. von Rieseemann
6449 K. D. Bergeron
6450 J. A. Reuscher
6451 T. F. Luera
6452 M. F. Aker
6453 W. J. Whitfield
6454 G. L. Cano (2)
7100 C. D. Broyles
7530 T. B. Lane
Attn: N. R. Keltner, 7537
R. U. Acton, 7537
T. Y. Chu, 7537
7550 F. W. Neilson
Attn: O. J. Burchett, 7551
J. H. Gieske, 7552
8424 M. A. Pound

| | | | | | |
|---|--|------------------------------------|--|---|--|
| NRC FORM 338 (2-84) NRCM 1102, 3201, 3202 | | U.S. NUCLEAR REGULATORY COMMISSION | | 1 REPORT NUMBER (Assigned by TRC and Va. No., if any) SAND81-0413 NUREG/CR-3662 | |
| SEE INSTRUCTIONS ON THE REVERSE | | | | | |
| 2 TITLE AND SUBTITLE Fuel-Disruption Experiments under High-Ramp-Rate Heating Conditions | | | | 3 LEAVE BLANK | |
| 5 AUTHOR(S) S. A. Wright, D. H. Worledge, G. L. Cano, P. K. Mast, F. Briscoe | | | | 4 DATE REPORT COMPLETED MONTH YEAR October 1983 | |
| 7 PERFORMING ORGANIZATION NAME AND MAILING ADDRESS (Include Zip Code) Division 6423 Sandia National Laboratories P. O. Box 5800 Albuquerque, NM 87185 | | | | 6 DATE REPORT ISSUED MONTH YEAR August 1984 | |
| 10 SPONSORING ORGANIZATION NAME AND MAILING ADDRESS (Include Zip Code) U. S. Nuclear Regulatory Commission Office of Nuclear Regulatory Research Division of Accident Evaluation Washington, DC 20555 | | | | 8 PROJECT TASK WORK UNIT NUMBER 9 FIN OR GRANT NUMBER A1016 | |
| 12 SUPPLEMENTARY NOTES | | | | 11 TYPE OF REPORT Technical | |
| 13 ABSTRACT (200 words or less) <p>This topical report presents the preliminary results and analysis of the High Ramp Rate fuel-disruption experiment series. These experiments were performed in the Annular Core Research Reactor at Sandia National Laboratories to investigate the timing and mode of fuel disruption during the prompt-burst phase of a loss-of-flow accident. High-speed cinematography was used to observe the timing and mode of the fuel disruption in a stack of five fuel pellets. Of the four experiments discussed, one used fresh mixed-oxide fuel, and three used irradiated mixed-oxide fuel.</p> <p>Analysis of the experiments indicates that in all cases, the observed disruption occurred well before fuel-vapor pressure was high enough to cause the disruption. The disruption appeared as a rapid spray-like expansion and occurred near the onset of fuel melting in the irradiated-fuel experiments and near the time of complete fuel melting in the fresh-fuel experiment. This early occurrence of fuel disruption is significant because it can potentially lower the work-energy release resulting from a prompt-burst disassembly accident.</p> | | | | 10 PERIOD COVERED (Include dates) 1980 | |
| 14 DOCUMENT ANALYSIS - KEYWORDS DESCRIPTORS fuel disruption, in-pile experiments, loss of flow, transient overpower, fission gas, liquid-metal fast-breeder reactor (LMFBR) | | | | 15 AVAILABILITY STATEMENT unlimited | |
| 16 IDENTIFIERS/OPEN ENDED TERMS | | | | 16 SECURITY CLASSIFICATION (This page) U | |
| | | | | (This report) U | |
| | | | | 17 NUMBER OF PAGES | |
| | | | | 18 PRICE | |